



Hydrodynamic Atmospheric Escape in HD 189733 b: Signatures of Carbon and Hydrogen Measured with the Hubble Space Telescope

Leonardo A. Dos Santos¹ , Antonio García Muñoz² , David K. Sing^{3,4} , Mercedes López-Morales⁵ , Munazza K. Alam⁶ , Vincent Bourrier⁷ , David Ehrenreich⁷ , Gregory W. Henry⁸ , Alain Lecavelier des Etangs⁹, Thomas Mikal-Evans¹⁰ ,

Nikolay K. Nikolov¹ , Jorge Sanz-Forcada¹¹ , and Hannah R. Wakeford¹²

¹ Space Telescope Science Institute, 3700 San Martin Drive, Baltimore, MD 21218, USA; ldsantos@stsci.edu

² Université Paris-Saclay, Université Paris Cité, CEA, CNRS, AIM, F-91191, Gif-sur-Yvette, France

³ Department of Physics and Astronomy, Johns Hopkins University, Baltimore, MD 21218, USA

⁴ Department of Earth & Planetary Sciences, Johns Hopkins University, Baltimore, MD, USA

⁵ Center for Astrophysics | Harvard & Smithsonian, 60 Garden Street, Cambridge, MA 02138, USA

⁶ Carnegie Earth & Planets Laboratory, 5241 Broad Branch Road NW, Washington, DC 20015, USA

⁷ Observatoire astronomique de l'Université de Genève, Chemin Pegasi 51, 1290 Versoix, Switzerland

⁸ Center of Excellence in Information Systems, Tennessee State University, Nashville, TN 37209, USA

⁹ Institut d'Astrophysique de Paris, CNRS, UMR 7095 & Sorbonne Universités UPMC Paris 6, 98bis bd Arago, 75014 Paris, France

¹⁰ Max Planck Institute for Astronomy, Königstuhl 17, D-69117 Heidelberg, Germany

¹¹ Departamento de Astrofísica, Centro de Astrobiología (CSIC-INTA), ESAC Campus, Camino bajo del Castillos s/n, E-28692 Villanueva de la Cañada, Madrid, Spain

¹² University of Bristol, HH Wills Physics Laboratory, Tyndall Avenue, Bristol, UK

Received 2023 April 11; revised 2023 June 14; accepted 2023 June 26; published 2023 August 3

Abstract

One of the most well-studied exoplanets to date, HD 189733 b, stands out as an archetypal hot Jupiter with many observations and theoretical models aimed at characterizing its atmosphere, interior, host star, and environment. We report here on the results of an extensive campaign to observe atmospheric escape signatures in HD 189733 b using the Hubble Space Telescope and its unique ultraviolet capabilities. We have found a tentative, but repeatable in-transit absorption of singly ionized carbon (C II, $5.2\% \pm 1.4\%$) in the epoch of June–July/2017, as well as a neutral hydrogen (H I) absorption consistent with previous observations. We model the hydrodynamic outflow of HD 189733 b using an isothermal Parker wind formulation to interpret the observations of escaping C and O nuclei at the altitudes probed by our observations. Our forward models indicate that the outflow of HD 189733 b is mostly neutral within an altitude of $\sim 2 R_p$ and singly ionized beyond that point. The measured in-transit absorption of C II at 1335.7 \AA is consistent with an escape rate of $\sim 1.1 \times 10^{11} \text{ g s}^{-1}$, assuming solar C abundance and an outflow temperature of 12,100 K. Although we find marginal neutral oxygen (O I) in-transit absorption, our models predict an in-transit depth that is only comparable to the size of measurement uncertainties. A comparison between the observed Ly α transit depths and hydrodynamics models suggests that the exosphere of this planet interacts with a stellar wind at least 1 order of magnitude stronger than solar.

Unified Astronomy Thesaurus concepts: [Exoplanet atmospheres \(487\)](#); [Hot Jupiters \(753\)](#); [Planet hosting stars \(1242\)](#); [Ultraviolet astronomy \(1736\)](#)

1. Introduction

One of the most striking discoveries in the search for exoplanets is that they can orbit their host stars at extremely close-in distances, a fact that initially challenged our understanding of planetary formation outside the solar system (see, e.g., the recent review by Zhu & Dong 2021). In particular, hot Jupiters were the first exoplanets to be found because they imprint strong transit and gravitational reflex signals in their host stars, despite their being intrinsically rare (Yee et al. 2021). Although as a community we ultimately aspire to find another planet similar to the Earth, hot Jupiters stand out as an important stepping stone because they are excellent laboratories to test our hypotheses of how planetary systems form and evolve (e.g., Fortney et al. 2021).

For small, short-period exoplanets, the impinging irradiation from their host stars and how it varies with time are some of the

most important factors that drive the evolution of their atmospheres (see, e.g., Owen 2019). That is because the incoming energetic photons (with wavelengths between X-rays and extreme-ultraviolet, or XUV) heat the upper atmosphere of the planet, which in turn expands and produces outflowing winds. If this outflow becomes supersonic, the atmospheric escape process is said to be hydrodynamic. Originally formulated by Watson et al. (1981) to describe the evolution of the early Earth and Venus, hydrodynamic escape has been observed in action in many hot exoplanets (e.g., Vidal-Madjar et al. 2003, 2004; Fossati et al. 2010; Sing et al. 2019). Other factors such as composition, as in atmospheres with high mean molecular weights, are also important in regulating the mass-loss rate of exoplanets (e.g., García Muñoz et al. 2021; Ito & Ikoma 2021; Nakayama et al. 2022).

The hot Jupiter HD 189733 b (Bouchy et al. 2005) is a particularly well-studied exoplanet owing to: (i) its proximity to the solar system, (ii) size and mass in relation to its host star, and (iii) short orbital period—see the stellar and planetary parameters in Table 1; these were compiled following the most recent and most complete datasets available in the literature, aiming for precision and consistency.

Original content from this work may be used under the terms of the [Creative Commons Attribution 4.0 licence](#). Any further distribution of this work must maintain attribution to the author(s) and the title of the work, journal citation and DOI.

Table 1
Stellar and Planetary Parameters, and Transit Ephemeris of the HD 189733 b System

Parameter	Unit	Value	References
Stellar radius	R_{\odot}	$0.765^{+0.019}_{-0.018}$	Addison et al. (2019)
Stellar mass	M_{\odot}	$0.812^{+0.041}_{-0.038}$	Addison et al. (2019)
Stellar effective temperature	K	5050 ± 20	Bonomo et al. (2019)
Projected rotational velocity	km s^{-1}	3.5 ± 1.0	Bonomo et al. (2017)
Age	Gyr	~ 1.2	Sanz-Forcada et al. (2010)
Systemic radial velocity	km s^{-1}	$-2.204^{+0.010}_{-0.011}$	Addison et al. (2019)
Distance	pc	$19.7638^{+0.0128}_{-0.0127}$	Gaia Collaboration et al. (2018)
Spectral type		K2V	Gray et al. (2003)
Planetary radius	R_{Jup}	1.119 ± 0.038	Addison et al. (2019)
Planet-to-star ratio	$R_{\text{p}}/R_{\text{s}}$	$0.1504^{+0.0038}_{-0.0039}$	Addison et al. (2019)
Planetary mass	M_{Jup}	$1.166^{+0.052}_{-0.049}$	Addison et al. (2019)
Planetary density	g cm^{-3}	$1.031^{+0.106}_{-0.090}$	Addison et al. (2019)
Planetary Equation temperature	K	1209 ± 11	Addison et al. (2019)
Orbital period	days	$2.218577^{+0.000009}_{-0.000010}$	Addison et al. (2019)
Semimajor axis	au	$0.03106^{+0.00051}_{-0.00049}$	Addison et al. (2019)
Orbital inclination	deg	$85.690^{+0.095}_{-0.097}$	Addison et al. (2019)
Eccentricity		< 0.0039	Bonomo et al. (2017)
Transit center reference time	BJD	$2458334.990899^{+0.000726}_{-0.000781}$	Addison et al. (2019)
Transit dur. (1st–4th contact)	hr	1.84 ± 0.04	Addison et al. (2019)

Note. The stellar and planetary parameters were obtained in the following DOI:[10.26133/NEA2](https://doi.org/10.26133/NEA2).

Previous optical observations of the atmosphere of HD 189733 b have shown that its transmission spectrum is consistent with the presence of high-altitude hazes (Lecavelier Des Etangs et al. 2008; Sing et al. 2011, 2016). In the near-infrared, the low amplitude of the water feature in transmission indicates a depletion of H_2O abundance from solar values, likely a result of its formation (Madhusudhan et al. 2014; McCullough et al. 2014). Using both transit and eclipse data of this planet, Zhang et al. (2020) concluded that the C/O ratio of HD 189733 b is ~ 0.66 and that it has a super-solar atmospheric metallicity.

Using different observational and theoretical techniques, previous atmospheric escape studies of HD 189733 b found that the planet likely has high mass-loss rates on the order of $10^{10}\text{--}10^{11} \text{ g s}^{-1}$, which is consistent with a hydrodynamic outflow (Lecavelier Des Etangs et al. 2010, 2012; Bourrier & Lecavelier des Etangs 2013; Salz et al. 2016a; Lampón et al. 2021). In this regime, the outflow of H is so intense that it can drag heavier species, such as C and O, upward to the exosphere of the planet, where these nuclei can quickly photoionize. In this context, Ben-Jaffel & Ballester (2013) reported on the detection of neutral oxygen (O I) in the exosphere of HD 189733 b, which the authors attribute to atmospheric escape, but require super-solar abundances and super-thermal line broadening to be explained; they also report the nondetection of singly ionized carbon (C II). More recently, Cubillos et al. (2023) ruled out the presence of singly ionized magnesium (Mg II) in the outflow of this planet and, although they reported the nondetection of Mg I, they did not rule out the presence of this species.

In this manuscript, we report on a comprehensive analysis of all far-ultraviolet (FUV) transit observations of HD 189733 b performed with the Hubble Space Telescope (HST) and the Cosmic Origins Spectrograph (COS) instrument obtained to date. In Section 2, we describe the observational setup and data reduction steps; Section 3 contains the results of our data analysis in the form of spectroscopic light curves; in Section 4,

we discuss the models we used to interpret our results and how they compare with the literature; in Section 5, we lay the main conclusions of this work.

2. Observations and Data Analysis

Several FUV transits of HD 189733 b have been observed with HST in the General Observer programs 11673 (PI: Lecavelier des Etangs), 14767 (PanCET program; PIs: Sing & López-Morales), and 15710 (PI: Cauley). Another program (12984, PI: Pillitteri) also observed HD 189733 in the frame of star–planet interactions, but no in-transit exposures were obtained. In program 15710, which aimed at measuring transits simultaneously with HST and ground-based facilities, two of three visits had guide-star problems and are not usable; the third visit has only one exposure covering in-transit fluxes, and the remaining ones occur after the transit; this nonoptimal transit coverage is likely the result of difficulties in coordinating HST and ground-based observatories for simultaneous observations. We list the dataset identifiers and times of observation in Table 2.¹³ Each identifier corresponds to one exposure of HST, or one orbit.

The COS observations were set to spectroscopic element G130M centered at 1291 Å and a circular aperture with a diameter of $2''/5$, yielding wavelength ranges [1134, 1274] Å and [1290, 1429] Å. The data were reduced automatically by the instrument pipeline (CALCOS version 3.3.11, which has corrected the bug with inflated uncertainties; Johnson et al. 2021). Several FUV transits of HD 189733 b have also been observed with the STIS spectrograph, but with a more limited wavelength range—thorough analyses of the STIS datasets are discussed in Lecavelier Des Etangs et al. (2012), Bourrier et al. (2013, 2020), and Barth et al. (2021). In this paper, we focus only on the COS data, which cover more metallic emission lines than the STIS data.

¹³ These data are openly available in the following DOI:[10.17909/2dq3-g745](https://doi.org/10.17909/2dq3-g745).

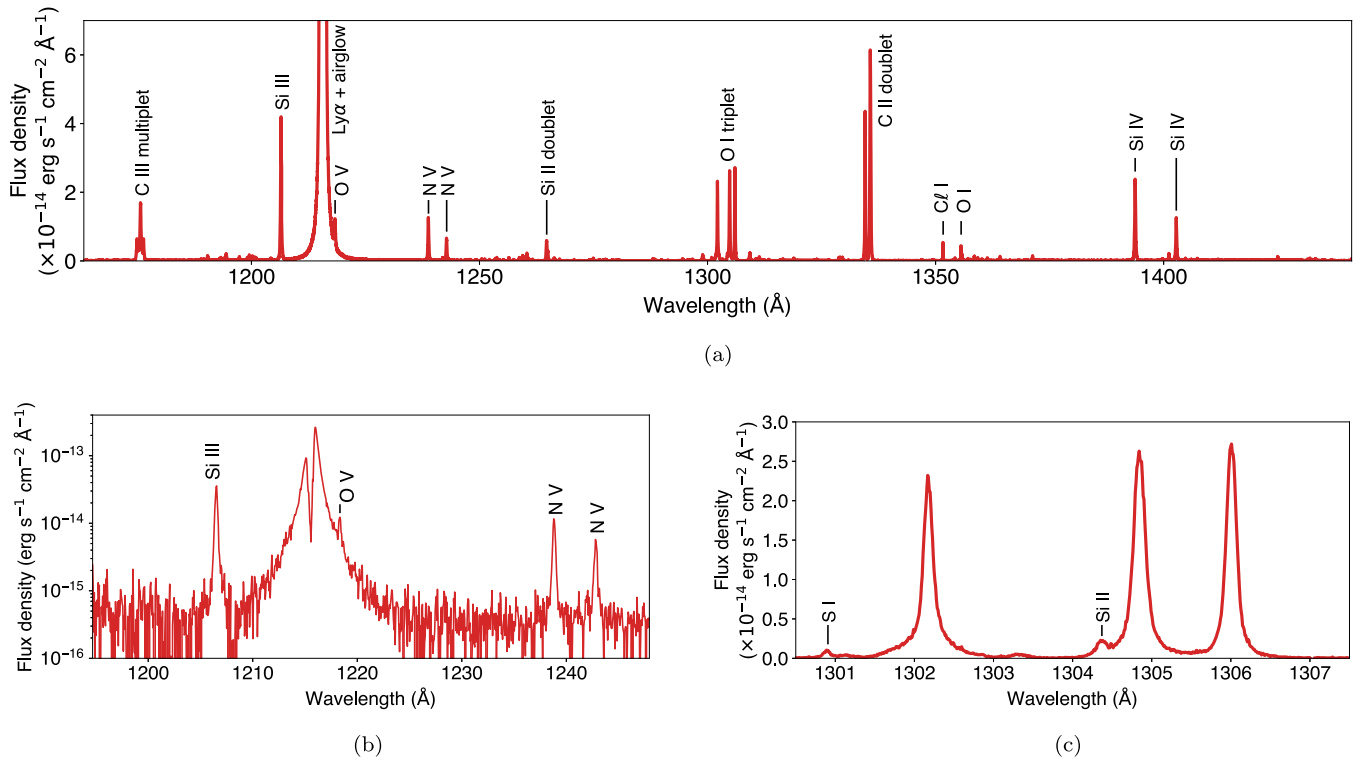


Figure 1. (a) Far-ultraviolet spectrum of HD 189733 measured with HST/COS in a combined exposure time of approximately 16 hr. (b) HST/STIS spectrum near the Ly α line. (c) Zoom in the COS spectrum in the wavelength range of the O I triplet.

Table 2
Observations Log of HD 189733 b Transits with HST/COS

Visit	Dataset	Start Time (BJD)	Exp. Time (s)	Phase
A	1b5k01ukq	2009-09-16 18:31:52.378	208.99	Out of transit
	1b5k01uoq	2009-09-16 19:50:49.344	889.18	Out of transit
	1b5ka1usq	2009-09-16 21:26:41.338	889.18	Out of transit
	1b5ka1uuq	2009-09-16 21:44:13.344	889.15	Ingress
	1b5ka1v2q	2009-09-16 23:02:33.331	889.15	In transit
	1b5ka1v4q	2009-09-16 23:20:05.338	889.18	Egress
	1b5ka1vmq	2009-09-17 00:38:25.325	889.18	Post-transit
	1b5ka1vpq	2009-09-17 00:55:57.331	889.18	Post-transit
B	1d9m50oxq	2017-06-24 08:03:55.843	2018.18	Out of transit
	1d9m50ozq	2017-06-24 09:24:16.877	2707.20	Out of transit
	1d9m50p1q	2017-06-24 10:59:38.803	2707.17	Ingress
	1d9m50p3q	2017-06-24 12:35:00.816	2707.17	Egress
	1d9m50p5q	2017-06-24 14:10:23.866	2707.17	Post-transit
C	1d9m51c1q	2017-07-03 05:00:55.786	2018.18	Out of transit
	1d9m51drq	2017-07-03 06:21:52.934	2707.20	Out of transit
	1d9m51duq	2017-07-03 07:57:12.960	2707.20	Ingress
	1d9m51dwq	2017-07-03 09:32:33.850	2707.20	Egress
	1d9m51dyq	2017-07-03 11:07:54.826	2707.20	Post-transit
D	1dzkh1ifq	2020-09-01 06:23:14.842	1068.16	In transit
	1dzkh1juq	2020-09-01 07:47:24.835	2060.19	Post-transit
	1dzkh1kbq	2020-09-01 09:22:43.824	2435.17	Post-transit
	1dzkh1l4q	2020-09-01 10:58:01.862	2600.19	Post-transit
	1dzkh1l7q	2020-09-01 12:33:20.851	2600.19	Post-transit

We search for signals of atmospheric escape using the transmission spectroscopy technique. Due to the strong oscillator strengths of FUV spectral lines, we analyze stellar emission lines individually (see Figure 1). In this regime, one

effective way of searching for excess in-transit absorption by an exospheric cloud around the planet is by measuring the light curves of fluxes in the emission lines (see, e.g., Vidal-Madjar et al. 2003; Ehrenreich et al. 2015; Dos Santos et al. 2019).

Depending on the abundance of a certain species in the exosphere, an excess absorption of a few to several percent can be detected.

The C II lines are a doublet with central wavelengths at 1334.5 Å and 1335.7 Å,¹⁴ both emitted by ions transitioning from the configuration $2s2p^2$ to the ground and first excited states of the configuration $2s^22p$, respectively. The O I lines are a triplet with central wavelengths at 1302.2 Å, 1304.9 Å, and 1306.0 Å, emitted by atoms transitioning from the configuration $2s^22p^3(^4S^o)3s$ to the ground, first excited, and second excited states of the configuration $2s^22p^4$, respectively. See the relative strengths of these spectral lines in Figure 1. As discussed in Bourrier et al. (2021), interstellar medium (ISM) absorption can in principle affect the observable flux of the C II lines. However, the effect is negligible for our analysis, which relies on a differential time-series analysis and not on the intrinsic stellar flux.

While analyzing the atomic oxygen (O I) lines, care has to be taken because of geocoronal contamination. To get around this issue, we subdivided the HST exposures into several subexposures, identifying which subexposures are contaminated, discarding them, and analyzing only the clean subexposures. As the O I contamination is correlated with the geocoronal emission levels in Ly α , we identify the problematic subexposures using the Ly α line, where the contamination is more obvious. When analyzing other emission lines that do not have geocoronal contamination, we do not discard any subexposures. In principle, the contamination in the O I lines can also be subtracted using templates in a similar fashion as the Ly α line (see Bourrier et al. 2018; Cruz Aguirre et al. 2023). However, the contrast between the airglow and the stellar emission of HD 189733 is too low to allow for a proper subtraction (see Appendix A); thus we opt to discard contaminated subexposures instead.

For relatively bright targets like HD 189733, the FUV continuum can be detected in COS spectroscopy despite the low signal-to-noise ratio (S/N). In our analysis, we measure the FUV continuum by integrating the COS spectra between the following wavelength ranges: [1165, 1173], [1178, 1188], [1338, 1346], [1372, 1392], [1413, 1424], and [1426, 1430] Å. These ranges strategically avoid strong emission lines and weaker ones that were identified by combining all available COS data (red spectrum in Figure 1).

3. Results

In the following discussion, we frequently mention fluxes during transit ingress and egress because those are the transit phases that are covered by Visits B and C (see Table 2). Visits A and D contain exposures near mid-transit, but the first visit has low S/N due to shorter exposure times and the latter does not have an adequate out-of-transit baseline. The light curves were normalized by the average flux in the exposures before the transit. As is customary in this methodology, we did not consider exposures after the transit as the baseline for normalization because they may contain post-transit absorption caused by an extended tail. The transit depths quoted in this manuscript are measured in relation to the baseline out-of-transit flux. In this section, we deem signals as detections

related to planet HD 189733 b if they are repeatable during transits in the epoch of 2017 (Visits B and C).

3.1. Exospheric Oxygen and Carbon

Upon inspection of the transit light curves represented in Figures 2 and 3, we found that HD 189733 b produces no significant in-transit absorption of neutral oxygen, but we measured repeatable absorption levels of ionized carbon at blueshifted Doppler velocities. Furthermore, some of these signatures are asymmetric in relation to the transit center, indicative of departures from spherical symmetry. In Section 4, we will see that no detectable atomic oxygen is expected in the exosphere of HD 189733 b.

For Visit A, we found that all exposures have low levels of geocoronal contamination except for the quarter of the following datasets: 1b5k01umq, 1b5ka1uqq, 1b5ka1v0q, and 1b5ka1vdq; these subexposures with high contamination were discarded from the O I analysis (see Appendix A). The exposures of Visits B, C, and D were longer, so we divided them into five subexposures instead of four. For Visits B and C, we discard the last subexposure of every dataset; in the case of 1d9m50oxq, we also discard the fourth subexposure. In Visit D, we discard the first subexposure of all exposures, except 1dzkh1lfq.

Our analysis of the O I light curves yields an in-transit absorption of $5.3\% \pm 1.9\%$ (2.8σ significance; Doppler velocity range $[-75, +75]$ km s⁻¹) by combining Visits B and C when co-adding all O I lines. In Visit A (epoch 2009), we do not detect a significant in-transit absorption, likely due to a combination of shorter exposure times and stellar variability (see Appendix B). We deem the results of Visit D (epoch 2020) inconclusive due to a nonoptimal out-of-transit baseline (see also Appendix B). We show the in- and out-of-transit O I spectra in the second and third rows of Figure 4.

In addition to O I, we also measure an in-transit absorption of singly ionized carbon (C II, all lines co-added) in HD 189733 b, more specifically $7.4\% \pm 2.0\%$ and $3.0\% \pm 2.1\%$ for Visits B and C, respectively. By combining these two visits, we measure an absorption of $5.2\% \pm 1.4\%$ (3.7σ detection; Doppler velocity range $[-100, +100]$ km s⁻¹). We report the ingress and egress absorption levels at different Doppler velocity ranges in Table 3. The signal is largely located in the blue wing, between velocities $[-100, 0]$ km s⁻¹, of the excited-state line at 1335.7 Å (see the top row of Figure 4); if the signal is indeed of planetary nature, this suggests that the material is being accelerated away from the host star (as seen in García Muñoz et al. 2021). The other emission lines in the COS spectrum (Si II, Si IV, C III, and N V) do not show significant variability (see Appendix B).

3.2. Nonrepeatable Signals: Stellar or Planetary Variability?

The hot Jupiter HD 189733 b is known for orbiting a variable host star and for having variable signatures of atmospheric escape (see, e.g., Bourrier et al. 2013; Cauley et al. 2018; Salz et al. 2018; Bourrier et al. 2020; Pillitteri et al. 2022; Zhang et al. 2022). Our analysis provides potential observational evidence for the variability of the upper atmosphere in this exoplanet, but it is difficult to disentangle it from variability in the host star emission-line flux.

In Visit B, the Si III line at 1206.5 Å shows a flux decrease of $7.6\% \pm 2.9\%$ near the egress of the transit (see left panel of Figure 5). This line is well known for being a sensitive tracer of

¹⁴ More specifically, there is a third component blended with the second line at 1335.66 Å, which would make this feature a triplet. However, this third component is 1 order of magnitude weaker than the second component.

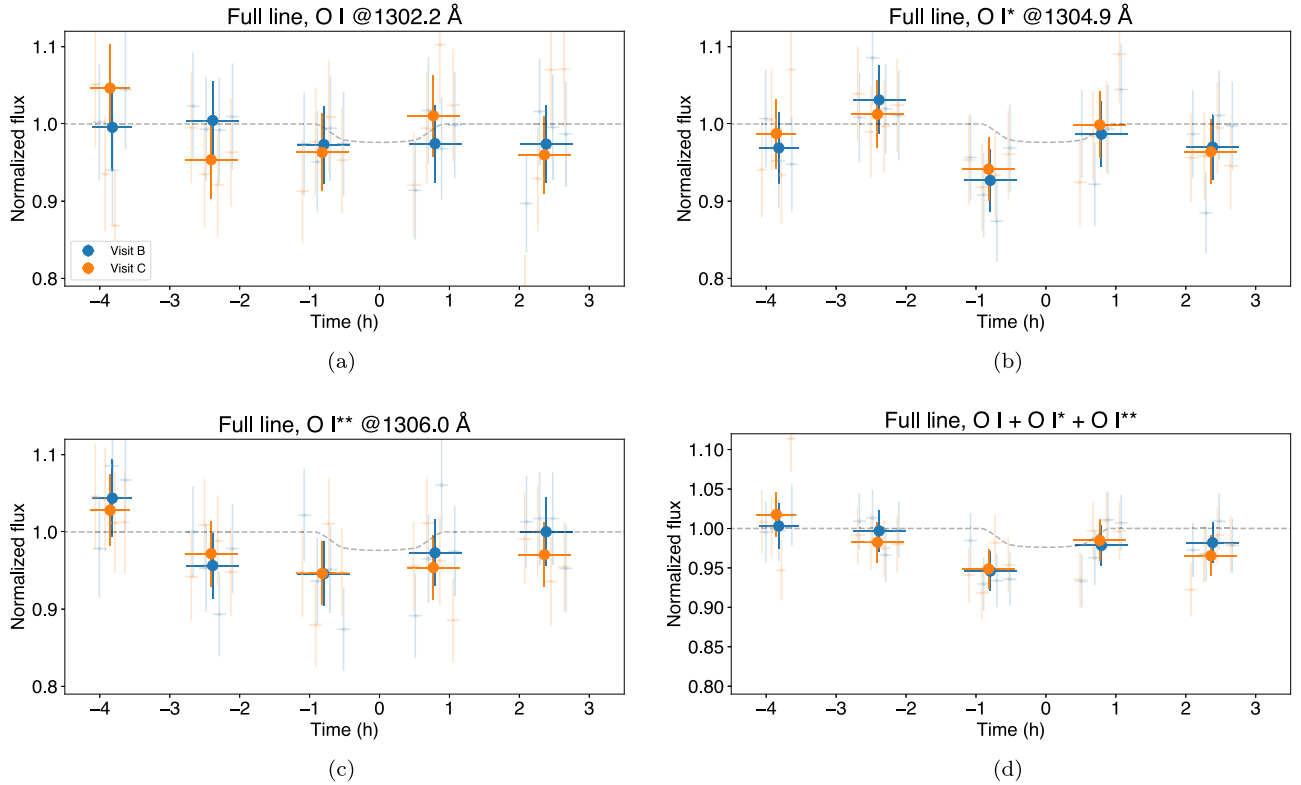


Figure 2. Neutral oxygen (O I) phase-folded transit light curves of HD 189733 b, split by the fine-structure lower level of the atom (here denoted by O I, O I*, and O I**). The dashed gray curve represents the transit of the planet as seen in optical wavelengths. Visits B and C are denoted by blue and orange filled circles, respectively, which correspond to epoch 2017. The semitransparent blue and orange measurements correspond to subexposures of Visits B and C. The light curves of Visits A and D, corresponding, respectively, to epochs 2009 and 2020, are shown in Appendix B.

stellar activity (e.g., Ben-Jaffel & Ballester 2013; Loyd & France 2014; Dos Santos et al. 2019; Bourrier et al. 2020). However, it is difficult to determine whether this signal is due only to stellar activity or the presence of doubly ionized Si in the upper atmosphere of HD 189733 b or a combination of both. Similar nonrepeatable egress absorptions are seen in the C II line at 1335.7 Å in Visit B. If it is due solely to stellar activity, it is possible that part of the in-transit absorption of C II observed in Visit B is also due to activity, as these lines are a moderate tracer of activity as well. With that said, it is not completely unexpected to see tails of ionized exospheric atoms after the egress of a highly irradiated planet like HD 189733 b (Owen et al. 2023). If the egress Si III flux decrease seen in Visit B is indeed due to the presence of doubly ionized Si in the exospheric tail of the planet, a nondetection in Visit C could be explained by: (i) variability in the outflow velocities of HD 189733 b, (ii) variability in its ionization level, or (iii) variation in the stellar wind. Further modeling will be necessary to test these different hypotheses, and we leave it for future efforts.

As the FUV continuum traces the lower chromosphere in solar-type stars (e.g., Linsky et al. 2012), we also compute its light curve and search for signals of variability connected to stellar activity. For HD 189733, we measure an average out-of-transit FUV continuum flux density of $(1.18 \pm 0.05) \times 10^{-16}$ and $(1.11 \pm 0.05) \times 10^{-16}$ erg s cm⁻² Å⁻¹, respectively, for visits B and C (see wavelength ranges in Section 2). The FUV continuum transit light curve is shown in the right panel of Figure 5. We do not detect statistically significant variability of the normalized FUV continuum flux during Visits B and C; however, the uncertainties of the measured fluxes are slightly larger than the line fluxes measured for the C II light curves.

Following the methods described in Dos Santos et al. (2019), we did not identify any flares in the datasets we analyzed and found no evidence for rotational or magnetic activity modulation of FUV fluxes due to the relatively short baseline of observations available. The photometric monitoring of the host star (see Appendix C) suggests a rotational period of 12.25 days. Visit B occurred during a time of maximum starspots, while Visit C occurred between times of maximum and minimum spottedness. In the HST data, we found that Visit B has higher absolute fluxes of metallic lines than Visit C by a factor of $\sim 10\%$ (except for Si II; see Appendix B). On the other hand, for the ground-based photometry in the *b* and *y* bands, we observe a Δmag of ~ 0.02 , which corresponds to a difference in flux of approximately 1.9% in the optical.

3.3. A Repeatable Hydrogen Signature

The COS spectra we analyze also contain information about the stellar Ly α line, despite the strong geocoronal contamination. We used the same technique described in Dos Santos et al. (2019) to remove the geocoronal contamination (see Appendix A) and analyzed the time series of the cleaned Ly α line for both its blue and red wings (respectively, $[-230, -140]$ km s⁻¹ and $[+60, +110]$ km s⁻¹, based on the results of Lecavelier Des Etangs et al. 2012). Some of the exposures in Visit A are not suitable for decontamination due to low S/N and had to be discarded. The resulting light curves are shown in Figure 6.

We found that the blue wing of the Ly α line shows a repeatable absorption during the ingress of HD 189733 b, with transit depths consistent between all visits. The light curves measured with COS are also consistent with that observed with

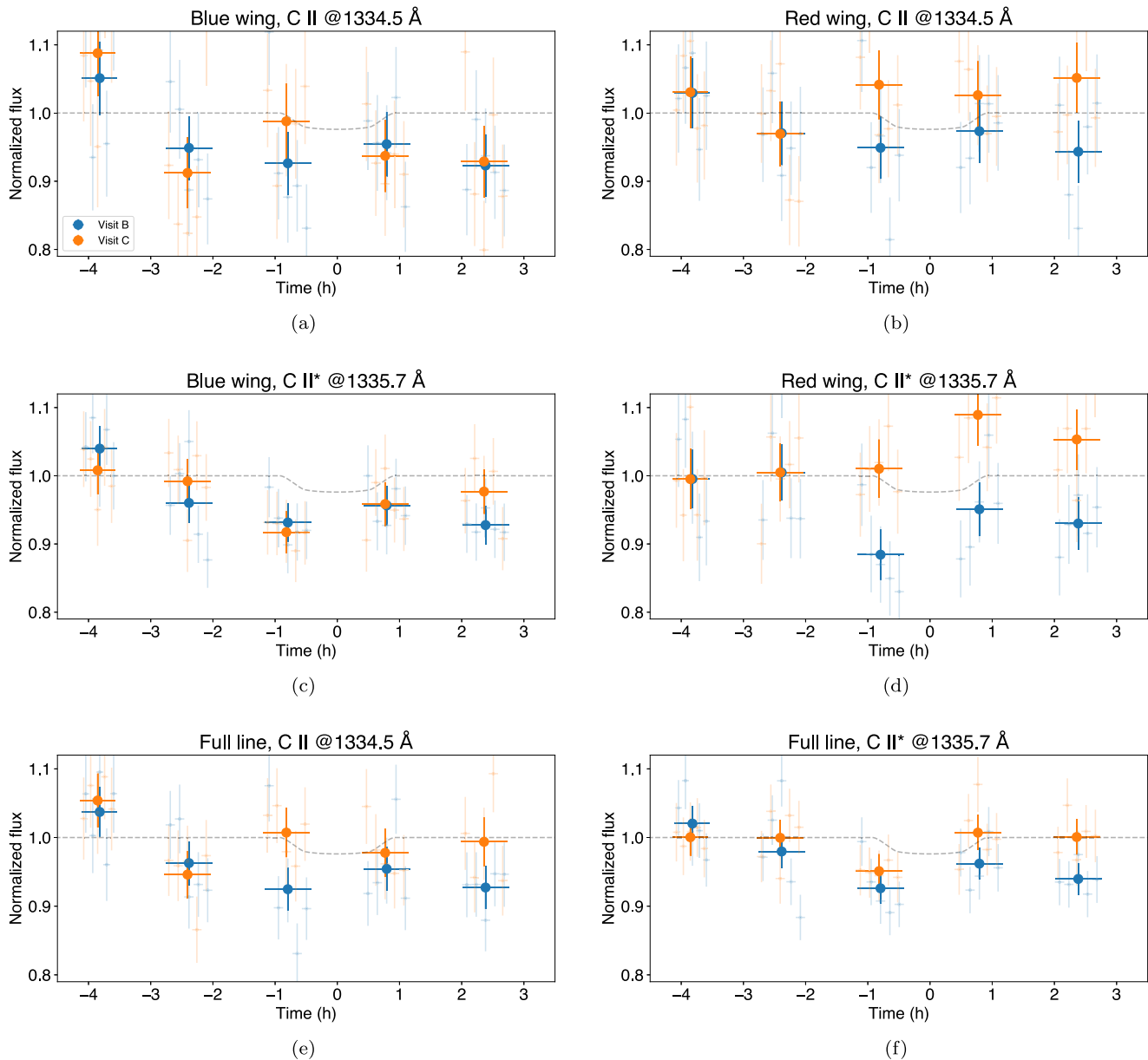


Figure 3. Same as Figure 2, but for singly ionized carbon (C II). Here we separate the light curves in blue and red wings, which are calculated by integrating the flux between Doppler velocities $[-100, 0]$ km s^{-1} and $[0, +100]$ km s^{-1} , respectively.

STIS (open circles in Figure 6; see also Bourrier et al. 2020). This signal at high velocities in the blue wing suggests that the exospheric H of HD 189733 b is accelerated away from the host star, an effect that has been extensively studied in, e.g., Bourrier & Lecavelier des Etangs (2013), Odert et al. (2020), and Rumenskikh et al. (2022). The time series of the Ly α red wing also shows an absorption during the transit of HD 189733 b. These results are consistent with the observations reported in Lecavelier Des Etangs et al. (2012).

In addition, we also found a hint of a post-transit absorption in the blue wing two hours after the transit mid-time, which could indicate the presence of a long neutral H tail as predicted by Owen et al. (2023). At this moment, it is unclear how consistent this would be with the doubly ionized Si tail hinted in the left panel of Figure 5, so we would benefit from future work in more detailed hydrodynamic modeling of HD 189733 b involving H and metallic species.

As we shall see in Section 4, our simplified one-dimensional modeling suggests that the exosphere of HD 189733 b is mostly ionized for all the species we simulated (H, He, C, and O). The detection of neutral H, however, is not inconsistent with this scenario, as even a small fraction of neutral H can yield a detectable signal due to the large absolute abundances of H atoms in the outflow.

The global three-dimensional hydrodynamics simulations presented by Rumenskikh et al. (2022) predict different levels of absorption in the blue and red wings of the Ly α line depending on the strength of the stellar wind (SW). According to their models, weaker winds ($\dot{M}_{\text{sw}} < 10^{13}$ g s^{-1})¹⁵ tend to produce deeper red-wing transits and shallower blue-wing absorption in the Doppler velocity ranges we analyzed. On the other hand, stronger winds ($\dot{M}_{\text{sw}} > 10^{13}$ g s^{-1}) produce transit

¹⁵ For comparison, the solar wind \dot{M} is $\sim 10^{12}$ g s^{-1} (Hundhausen 1997).

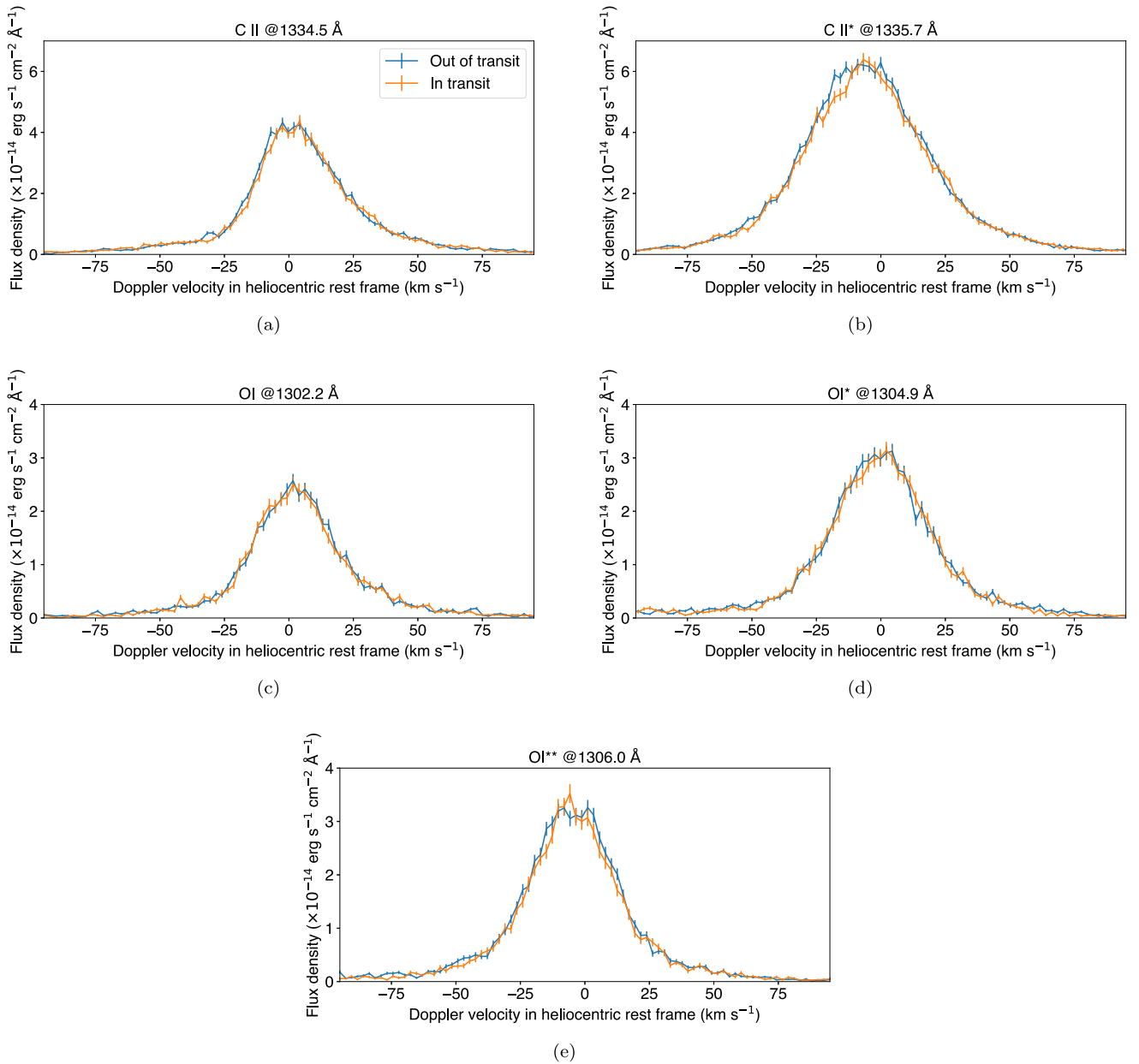


Figure 4. In-transit and out-of-transit spectra of HD 189733 for the C II and O I lines. In this plot we consider that datasets 1d9m50p1q, 1d9m50p3q, 1d9m51duq, and 1d9m51dwq are in transit, and the remaining datasets from Visits B and C are out of transit. We did not include Visits A and D in this combined spectrum. The in-transit absorption in the excited-state C II* line is seen in its blue wing.

depths that are similar to those that we measured in both blue and red wings. These results highlight the importance of Ly α transits to study not only exoplanet outflows but also their interaction with the stellar wind.

4. Modeling the Escape of Carbon and Oxygen

To interpret our observations, we produce forward models of the escaping atmosphere of HD 189733 b using the code *p-winds* (version 1.4.4;¹⁶ Dos Santos et al. 2022). The code calculates the structure of the planet’s upper atmosphere by assuming that the outflow can be simulated as an isothermal, one-dimensional Parker wind (Parker 1958). We further assume that the planet’s atmosphere has a H/He fraction of

90/10, and that C and O are trace elements. In this version of *p-winds*, the code computes the ionization–advection balance using the photoionization, recombination, and charge transfer reactions listed in Table 1 of Koskinen et al. (2013). We further include the charge transfer reaction between C²⁺ and He⁰ from Brown (1972). A more detailed description of this version of the code is present in Appendix D. We caution that our simulation is simplified in that we assume that the outflow is one-dimensional; a more accurate model for an asymmetric transit would require three-dimensional modeling. As the focus of this manuscript is on reporting the results of the observation, we provide here only this simplified modeling approach and leave more detailed modeling for future work.

The distribution of ions in the upper atmosphere of an exoplanet is highly dependent on the incident high-energy spectral energy distribution (SED) from the host star. For the

¹⁶ DOI:10.5281/zenodo.7814782.

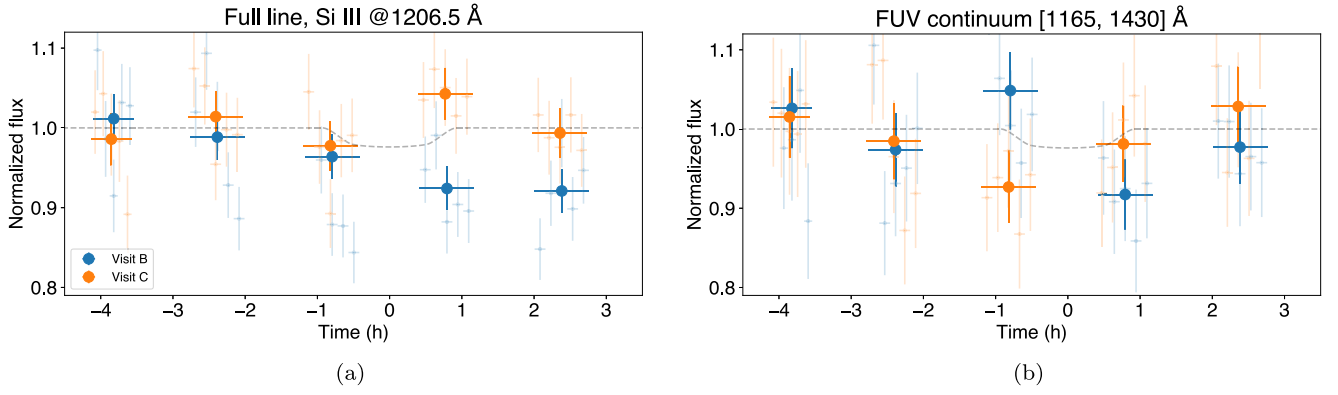


Figure 5. Left panel: transit light curve of doubly ionized silicon, a line that is sensitive to stellar activity modulation. Right panel: transit light curve of the FUV continuum (excluding emission lines, Ly α wings, and the detector gap).

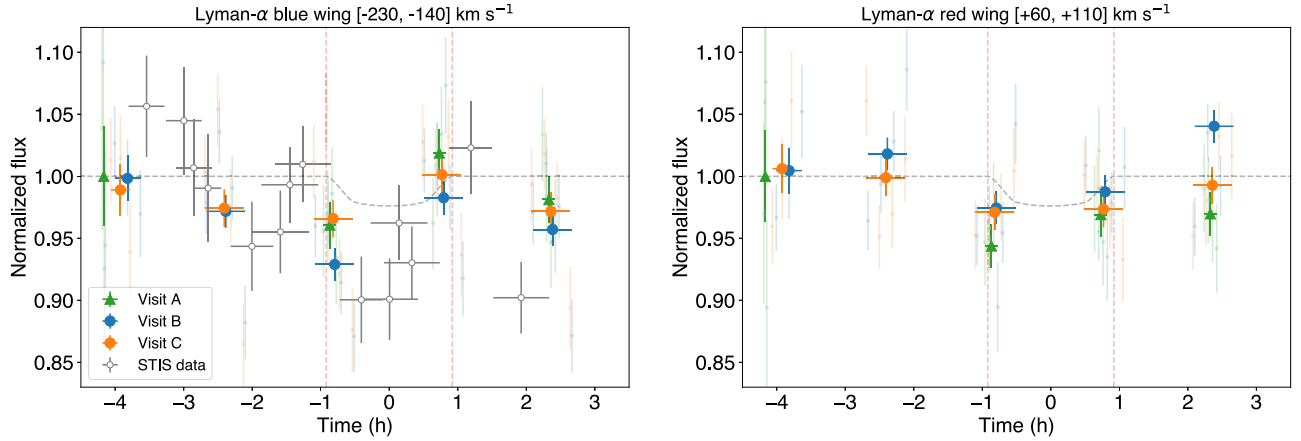


Figure 6. Ly α transit light curves of HD 189733 b measured with COS (full symbols) and STIS (open circles). The green symbols correspond to Visit A, and the blue and orange symbols correspond to Visits B and C, similar to the other light curves shown in this manuscript. We detect a repeatable absorption in the Ly α blue wing (left panel) attributed to the presence of escaping H in Visits A and B, which are consistent with the one previously measured with STIS (see Bourrier et al. 2020). No in-transit absorption is detected in Visit C, reinforcing that the exospheric H in the planet is variable. We also observe a variable in-transit absorption in the red wing with COS (right panel).

Table 3

Average in-transit Absorption Levels Measured over Visits B and C

Species	Blue Wing	Red Wing	Full Line
Ingress			
O I	2.3% \pm 5.5%	5.1% \pm 5.1%	3.2% \pm 3.7%
O I*	8.9% \pm 4.2%	1.6% \pm 4.7%	6.6% \pm 3.1%
O I*	3.4% \pm 3.9%	9.9% \pm 5.5%	5.4% \pm 3.1%
C II	4.3% \pm 3.7%	0.5% \pm 3.4%	3.4% \pm 2.4%
C II*	7.6% \pm 2.3%	5.3% \pm 3.0%	6.1% \pm 1.8%
Egress			
O I	5.5% \pm 5.5%	-0.1% \pm 5.1%	0.7% \pm 3.7%
O I*	1.5% \pm 4.2%	0.1% \pm 4.7%	0.7% \pm 3.1%
O I*	0.0% \pm 3.9%	8.6% \pm 5.4%	3.7% \pm 3.1%
C II	5.4% \pm 3.7%	0.0% \pm 3.4%	3.4% \pm 2.4%
C II*	4.2% \pm 2.2%	-2.0% \pm 3.0%	1.5% \pm 1.8%

Note. Visits A and D were excluded from this analysis because they were observed in different epochs from the PanCET visits (see details in Section 2).

purposes of this experiment, we will use the high-energy SED of HD 189733 that was estimated in Bourrier et al. (2020), based on X-rays and HST observations.

We calculate the expected distributions of C II and O I as a function of the altitude by assuming that the planet has solar C

and O abundances, the escape rate¹⁷ is $1.7 \times 10^{10} \text{ g s}^{-1}$, and the outflow temperature is 11 800 K based on the comprehensive one-dimensional hydrodynamic simulations of Salz et al. (2016a); we refer to this setup as Model 1 or M1. We also produce a forward model assuming solar C and O abundances, an escape rate of $1.1 \times 10^{11} \text{ g s}^{-1}$, and an outflow temperature of 12,400 K, which were estimated by fitting the metastable He transmission spectrum of HD 189733 b (Lampón et al. 2021); we refer to this setup as Model 2 or M2. Finally, we also calculate a forward model based on the photochemical formalism presented in García Muñoz (2007), which yields an escape rate of $1.8 \times 10^{10} \text{ g s}^{-1}$ and a maximum thermospheric temperature of 12,000 K; we refer to this setup as Model 3 or M3.

Our results for M1 and M2 show that the upper atmosphere of HD 189733 b is mostly neutral within altitudes of $\sim 2 R_p$ for all species: H, He, C, and O; beyond this point, the atmosphere is predominantly singly ionized (see left panels of Figure 7). For M3, we found that the outflow is mostly singly ionized and is

¹⁷ When referring to mass-loss rates in this manuscript, we are referring to the substellar escape rate. The term “substellar” is used when assuming that the planet is irradiated over $4\pi \text{ sr}$. This assumption is usually employed in one-dimensional models like *p-winds*. In reality, planets are irradiated over $\pi \text{ sr}$ only, and the total mass-loss rate is obtained by dividing the substellar rate by 4.

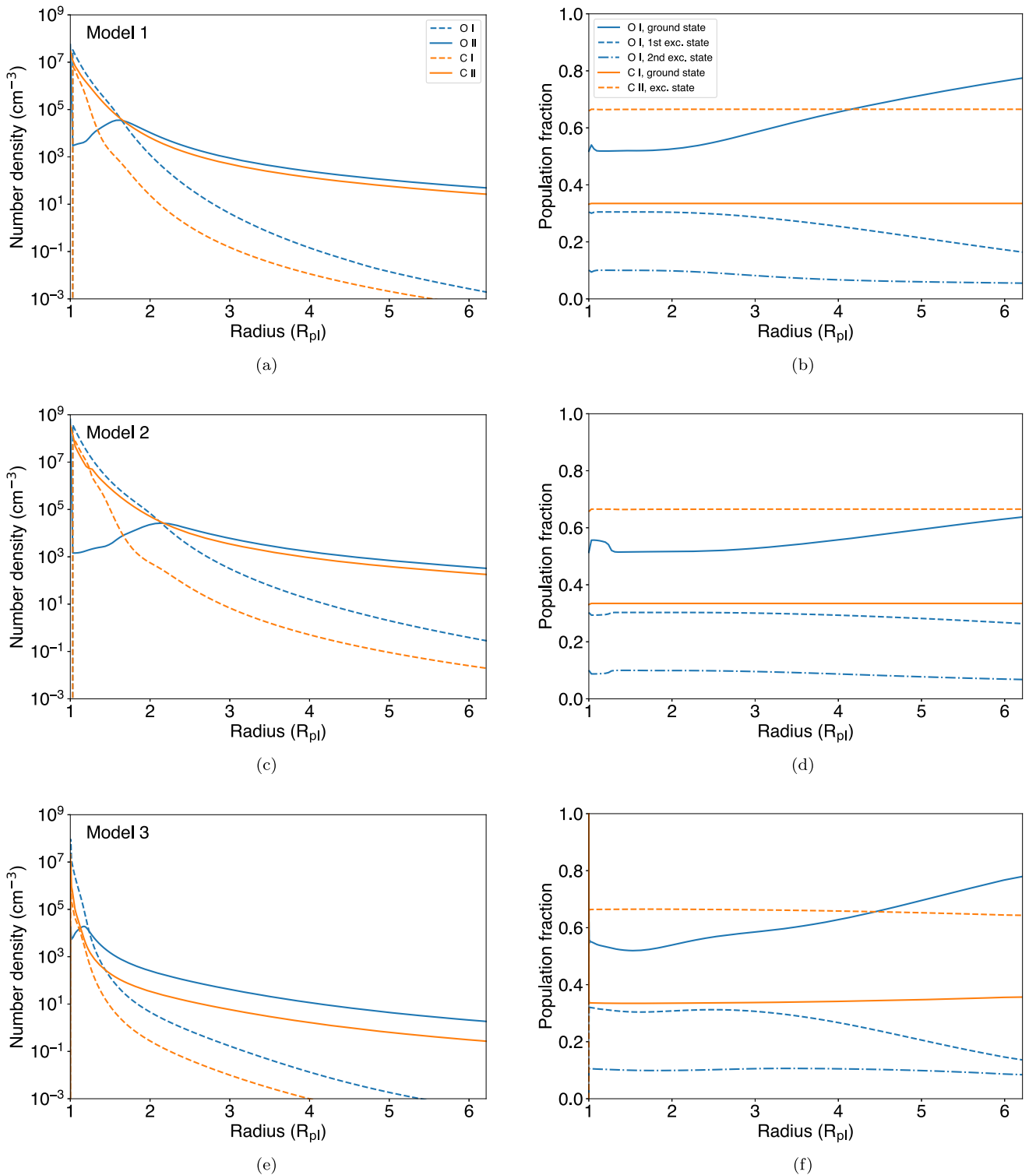


Figure 7. (a) Distribution of neutral (dashed lines) and singly ionized (full lines) carbon (orange) and oxygen (blue) in the upper atmosphere of HD 189733 b. The outflow of HD 189733 b is mostly singly ionized, and no doubly ionized C is produced. (b) Distribution of the different excitation levels of C and O, with the full, dashed, and dotted-dashed lines indicating, respectively, the ground, first excited, and second excited states, respectively. Panels (a) and (b) assume the escape rate and outflow temperature estimated by Salz et al. (2016a). Panels (c) and (d) are the same as (a) and (b), but assuming the escape rate and outflow temperature estimated by Lampón et al. (2021). Panels (e) and (f) correspond to the photochemical model described in García Muñoz et al. (2021).

neutral only near the base of the wind. The population of ground and excited states C and O is sensitive to the assumed mass-loss rate and outflow temperature because they control how many electrons are available to collide and excite the nuclei, as well as the energy of the electrons (see right panels of Figure 7).

We used the density profiles of O I and C II, as well as the ground/excited-state fractions to calculate the expected transmission spectra of HD 189733 b near the ingress of the planet, where we found the strongest signals of a possible in-transit planetary absorption (see Figure 3). To this end, we used

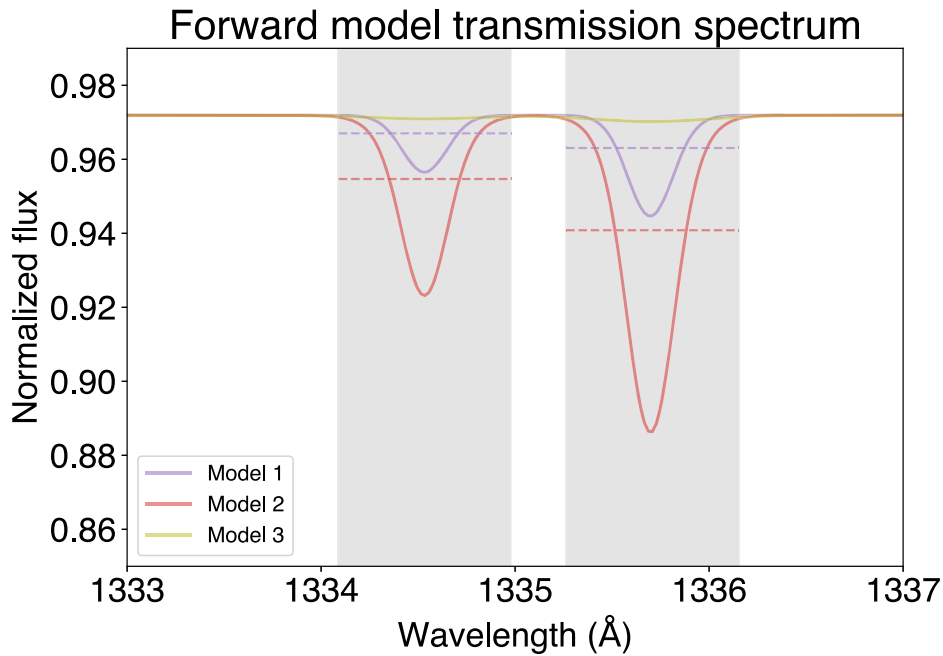


Figure 8. Simulated ingress transmission spectra of HD 189733 b near the C II triplet in the UV. The shaded region delimits the wavelength ranges in which the flux density is integrated to calculate the light curves seen in Figure 3. The dashed horizontal lines indicate the average ingress absorption in the wavelength range delimited by the shaded region and correspond to the absorption levels in Table 4. See a description of the different models in the main text.

Table 4
Wavelength-averaged Ingress Absorption Calculated for our Models

Species	Model 1	Model 2	Model 3
O I (all lines)	3.0%	3.3%	3.0%
C II	3.3%	4.5%	2.9%
C II*	3.6%	5.9%	2.9%

the instrumental line spread function of the COS with the G130M grating centered at $\lambda_0 = 1291 \text{ \AA}$ obtained from STScI.¹⁸ The resulting theoretical transmission spectra are shown in Figure 8.

In order to compare these predictions with our observations, we take the average in-transit absorption within limited integration ranges where there is a detectable stellar flux in each wavelength bin. These ranges are the Doppler velocities $[-100, +100] \text{ km s}^{-1}$ in the stellar rest frame for C II and $[-75, +75] \text{ km s}^{-1}$ for O I. The results are shown in Table 4.

As expected for the lower mass-loss rate inferred by Salz et al. (2016a; $1.7 \times 10^{10} \text{ g s}^{-1}$) and by M3 ($1.8 \times 10^{10} \text{ g s}^{-1}$) as compared to the estimate of Lampón et al. (2021), the excess absorptions in M1 and M3 are shallower than that of M2 and are inconsistent with the C II transit depths that we observe with COS. We find that an isothermal Parker wind model with an escape rate of $1.1 \times 10^{11} \text{ g s}^{-1}$, estimated from metastable He spectroscopy (Lampón et al. 2021), yields a C II transit depth that is consistent with the COS observations. This mass-loss rate is also consistent with the simple estimates from Sanz-Forcada et al. (2011), based on the energy-limited formulation (Salz et al. 2016b). As seen in Table 4, all models predict an O I transit depth of approximately 3%, which is comparable to the sizes of the uncertainties of the COS transit depths.

Considering that M2 has a solar H fraction of 90% and yields an average neutral fraction of 26%, we estimate that the substellar escape rate of neutral H is $2.6 \times 10^{10} \text{ g s}^{-1}$. As the planet is irradiated only over $\pi \text{ sr}$, we divide the substellar rate by 4, yielding $6.4 \times 10^9 \text{ g s}^{-1}$. This escape rate of neutral H is comparable to that estimated by Lecavelier Des Etangs et al. (2012) and Bourrier & Lecavelier des Etangs (2013) from Ly α transit observations. Our simulations are also consistent with the hydrodynamic models calculated by Ben-Jaffel & Ballester (2013), which predict an O I transit depth of about 3.5%. However, Ben-Jaffel & Ballester (2013) claimed that super-solar O abundances or super-thermal broadening or the absorption lines are required to fit the $\sim 6.4\%$ transit depth they had measured for O I. As we did not find such a deep O I transit in our analysis, no changes in the assumptions of our models were necessary.

5. Conclusions

We reported on the analysis of several HST transit spectroscopy observations of HD 189733 b in the FUV. We found a tentative, but repeatable absorption of $6.1\% \pm 1.8\%$ in the singly ionized carbon line in the first excited state during the June–July/2017 epoch. This signal is in tension with the 2009 observations of this planet, which found no significant in-transit absorption of C II. In addition, we found a less significant ingress absorption in the neutral oxygen lines of $5.3\% \pm 1.9\%$.

Our analysis yielded hints of a C II and Si III post-transit tail, but they are not repeatable across the visits in question. We could not draw a definitive conclusion about whether these nonrepeatable signals are due to planetary or stellar variability. Although we were able to measure the FUV continuum flux of HD 189733 using COS, its light curves show no signal of significant in-transit absorption or variability. A comparison between absolute FUV fluxes and nearly simultaneous ground-based photometry in the *b* and *y* bands suggests that FUV

¹⁸ <https://www.stsci.edu/hst/instrumentation/cos/performance/spectral-resolution>

emission lines tend to increase in flux by a factor of 10% when the star is 1.9% fainter in the optical due to starspots.

Using a geocoronal decontamination technique, we analyzed the Ly α time series and found a repeatable in-transit absorption in both the blue and red wings of the stellar emission. This result is consistent with previous studies using the STIS spectrograph. A comparison with hydrodynamics models in the literature shows that the Ly α absorption levels we found are consistent with an outflow that interacts with a stellar wind at least 10 times stronger than solar.

We interpreted the tentative C II and O I signals using the one-dimensional, isothermal Parker wind approximation of the Python code `p-winds`, which was originally created for metastable He observations. We adapted this code to include the photochemistry of C and O nuclei (see Appendix D). This adaptation is publicly available as `p-winds` version 1.4.3. Based on our modeling, we conclude that the mass-loss rate of HD 189733 b is consistent with those inferred by the previous observational estimates of Bourrier & Lecavelier des Etangs (2013; neutral H escape rate of $\sim 10^9$ g s $^{-1}$) and Lampón et al. (2021; total escape rate of 1.1×10^{11} g s $^{-1}$), assuming solar abundances for the planet. Interestingly, for exoplanets that we detect both C and O escaping, we may be able to measure the C/O ratio of the outflow and compare them with estimates obtained with near-infrared transmission spectra measured with the JWST.

We will benefit from future modeling efforts to address the following open questions: (i) What levels of stellar variability in its wind and high-energy input are necessary to produce variability in the planetary outflow? How can we observationally disentangle them? (ii) Does HD 189733 b possess a post-transit tail with neutral H and ionized C and Si?

Acknowledgments

L.A.D.S. thanks the postdoctoral researchers of STScI, Aline Vidotto, and Ofer Cohen for their helpful input during the writing of this manuscript and acknowledges the often-overlooked labor of the custodial, facilities, and security staff at STScI—this research would not be possible without them. L. A.D.S. further thanks Shreyas Vissapragada and Michael Gully-Santiago for contributing to the `p-winds` code, and

Dion Linssen, Lars Klijn, and Yassin Jaziri for helping find bugs in the code. The authors thank the anonymous referee for the kind and valuable feedback given to this manuscript. A.L. D.E. acknowledges support from the CNES (Centre National D'études Spatiales, France). This work is part of the HST Panchromatic Comparative Exoplanetary Treasury (PanCET) Program GO-14767. Astronomy at Tennessee State University is supported by the State of Tennessee through its Centers of Excellence program. This research was enabled by financial support from the European Research Council (ERC) under the European Union's Horizon 2020 research and innovation program (projects: FOUR ACES grant agreement No. 724427 and SPICE DUNE grant agreement No. 947634), and it has been carried out in the frame of the NCCR PlanetS supported by the Swiss National Science Foundation under grants 51NF40_182901 and 51NF40_205606. This research is based on observations made with the NASA/ESA Hubble Space Telescope. The data are openly available in the Mikulski Archive for Space Telescopes (MAST), which is maintained by the Space Telescope Science Institute (STScI). STScI is operated by the Association of Universities for Research in Astronomy, Inc. under NASA contract NAS 5-26555. STScI stands on the traditional and unceded territory of the Piscataway-Conoy and Susquehannock peoples. This research made use of the NASA Exoplanet Archive, which is operated by the California Institute of Technology, under contract with the National Aeronautics and Space Administration under the Exoplanet Exploration Program.

Facilities: HST(STIS), HST(COS).

Software: NumPy (Harris et al. 2020), SciPy (Virtanen et al. 2020), Astropy (Astropy Collaboration et al. 2018), Jupyter (Kluyver et al. 2016), Matplotlib (Hunter 2007), `p-winds` (Dos Santos et al. 2022), ChiantiPy (Landi et al. 2012), `batman` (Kreidberg 2015).

Appendix A Airglow Removal from COS Spectroscopy

The geocoronal contamination in COS spectra extends over a wide wavelength range near the Ly α and O I lines and, as opposed to STIS, it is not easily subtracted by the instrument's pipeline. The reason for that is because of a combination of the

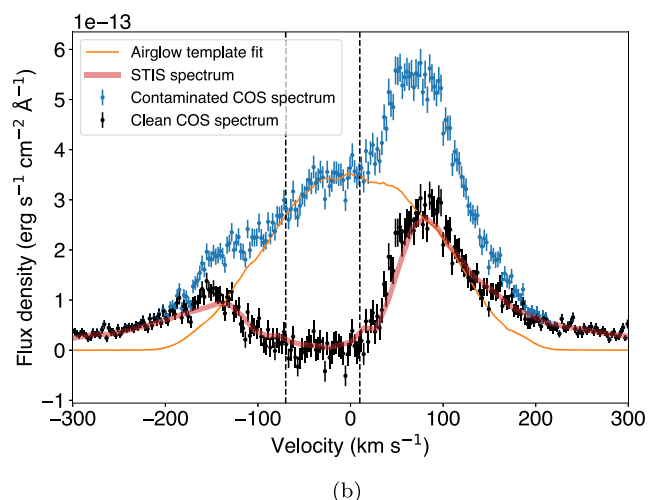
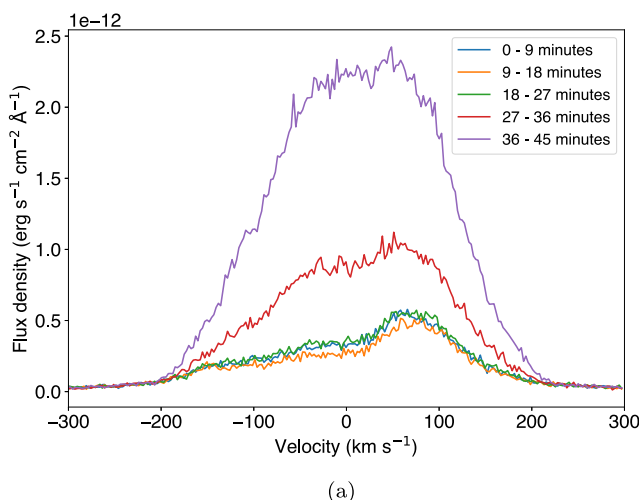


Figure 9. (a) Example of the varying levels of geocoronal contamination depending on the time of the subexposure in a given orbit; we show here the subexposures from dataset 1d9m50ozq. (b) Example of one Ly α geocoronal contamination removal using airglow templates. The subexposure shown here corresponds to the first quarter of dataset 1d9m50ozq. Velocities are in the heliocentric rest frame.

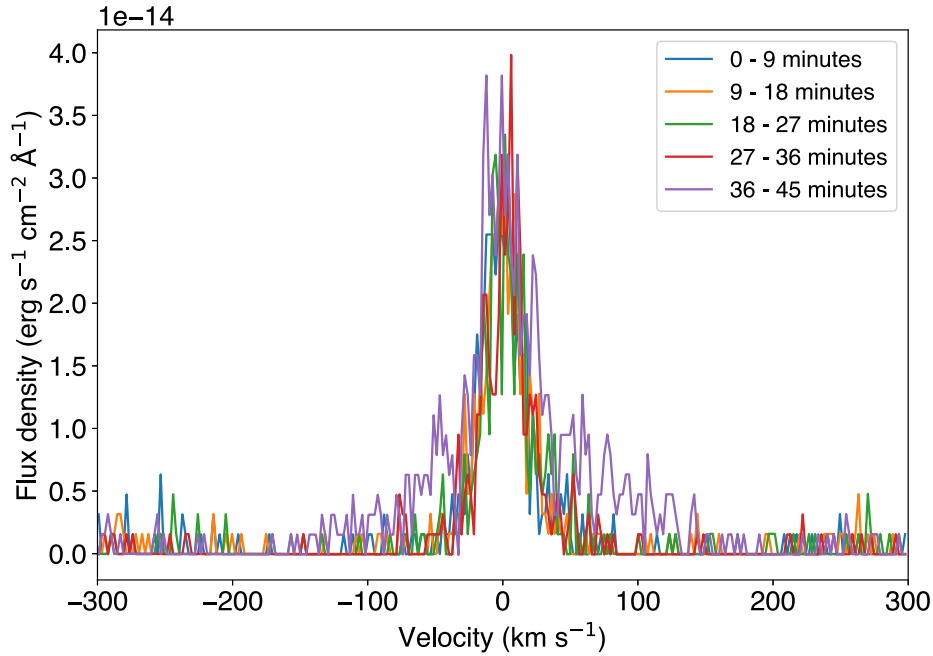


Figure 10. Example of O I geocoronal contamination in five subexposures of dataset 1d9m50ozq, observed as a wider contribution to narrow stellar emission line. By comparison with the left panel of Figure 9, we conclude that the level of O I contamination correlates with the Ly α geocoronal contamination.

large angular size of its circular aperture and the fact that it does not acquire angularly resolved spectra away from the science target that would serve as a sky background (Green et al. 2012). However, it is possible to subtract this contamination with some careful analysis after the data reduction. A detailed description of this process is discussed in Dos Santos et al. (2019; see also Cruz Aguirre et al. 2023). Briefly, for Ly α , it consists of identifying a wavelength range where we do not expect stellar emission, such as the core of the stellar Ly α line (which is absorbed by the interstellar medium and thus contain only geocoronal emission). Then, we fit an airglow template¹⁹ with varying amplitudes and wavelength shifts to this region without stellar emission. In the case of our observation, we found that the best range to fit the airglow templates was $[-70, +10]$ km s⁻¹ in the heliocentric rest frame. We illustrate this process in Figure 9.

We verified that, for Visits A, B, and C, each COS full exposure is comprised of one or more subexposures that have relatively low levels of contamination (see the blue, orange, and red spectra in the left panel of Figure 9). We use these subexposures to build clean O I profiles, as geocoronal contamination in these lines is negligible in the regime of low airglow (see an example in Figure 10).

Appendix B Additional Light Curves

We include here light curves of O I and C II for Visits A and D (see Figure 11), as well as light curves of C III, Si II, Si IV, and N V for all visits (see Figure 12). The absolute-flux light curves of the host star are shown in Figure 13.

¹⁹ COS airglow templates are publicly available in <https://www.stsci.edu/hst/instrumentation/cos/calibration/airglow>.

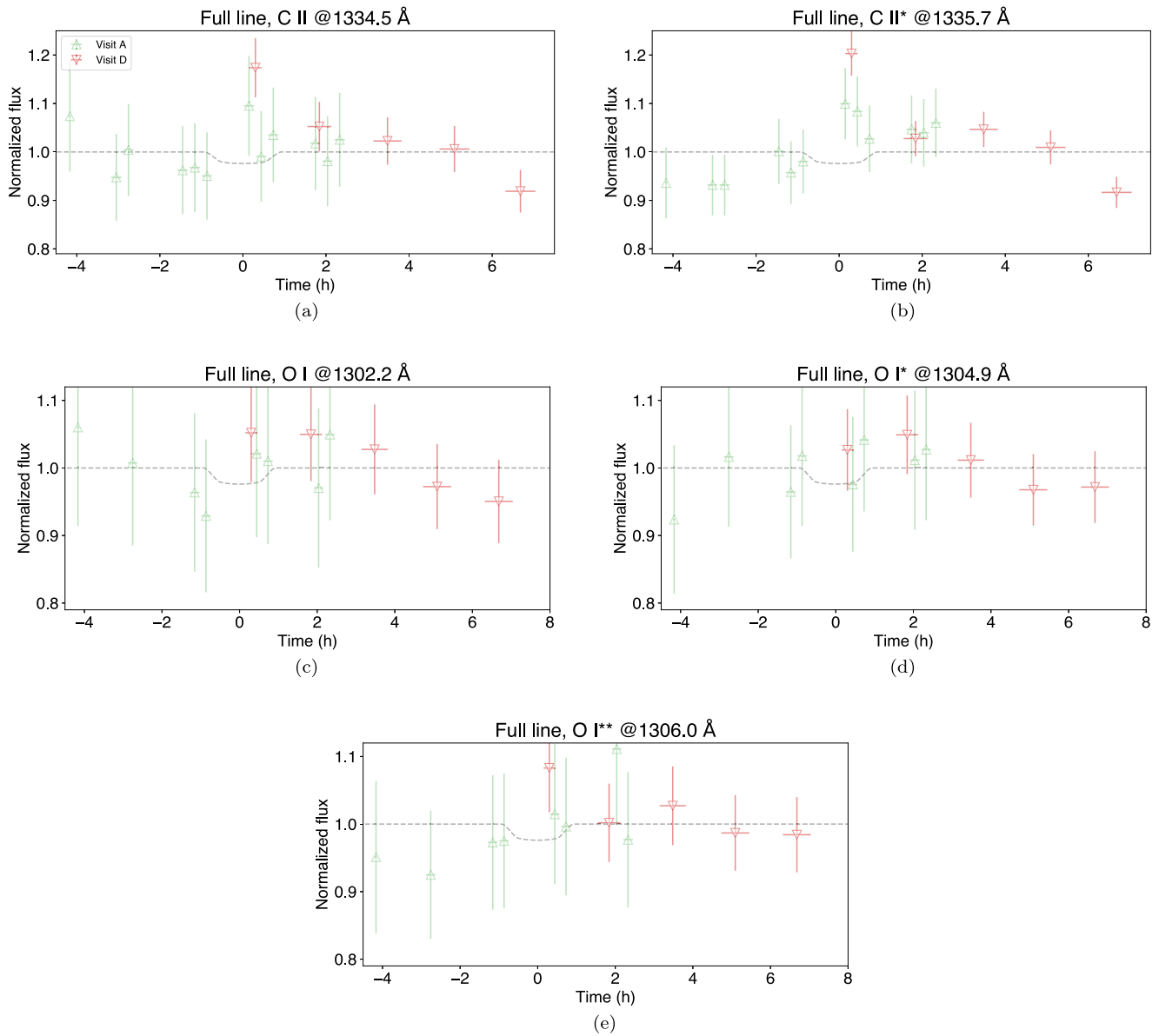


Figure 11. Transit light curves of HD 189733 b in Visits A and D for the O I and C II lines present in COS spectra.

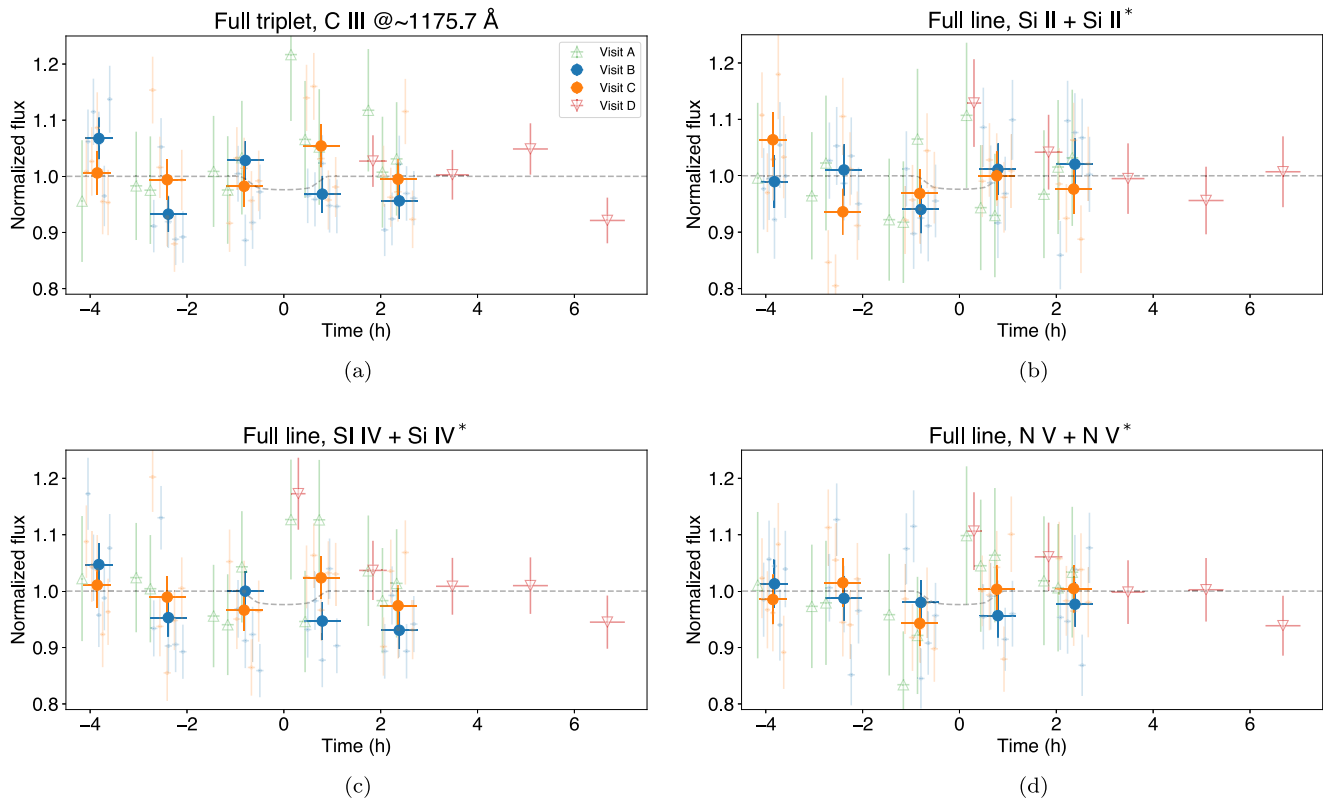


Figure 12. Additional transit light curves of HD 189733 b for other lines of metallic species present in COS spectra.

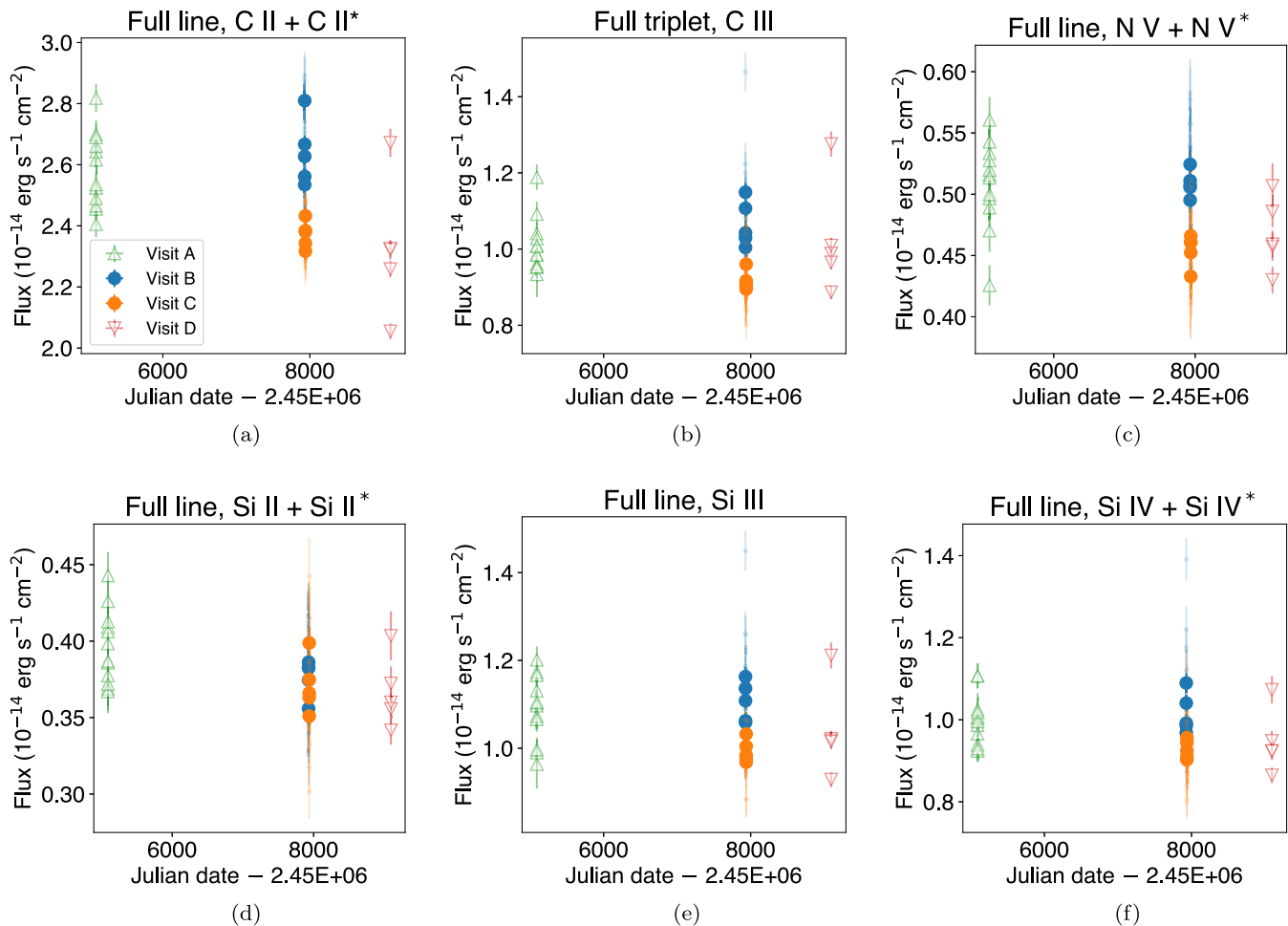


Figure 13. Absolute-flux light curves of HD 189733 for lines of metallic species present in the COS spectra.

Appendix C

Ground-based Photometric Monitoring of HD 189733

We acquired photometric observations of HD 189733 during 2017A with the T10 0.80 m automatic photoelectric telescope (APT) at Fairborn Observatory in Arizona. The T10 APT is

equipped with a two-channel photometer that uses two EMI 9124QB bi-alkali photomultiplier tubes to measure stellar brightness simultaneously in the Strömgen *b* and *y* passbands.

The photometry of HD 189733 was measured differentially with respect to the nearby comparison star HD 191260. To improve the photometric precision of the individual nightly

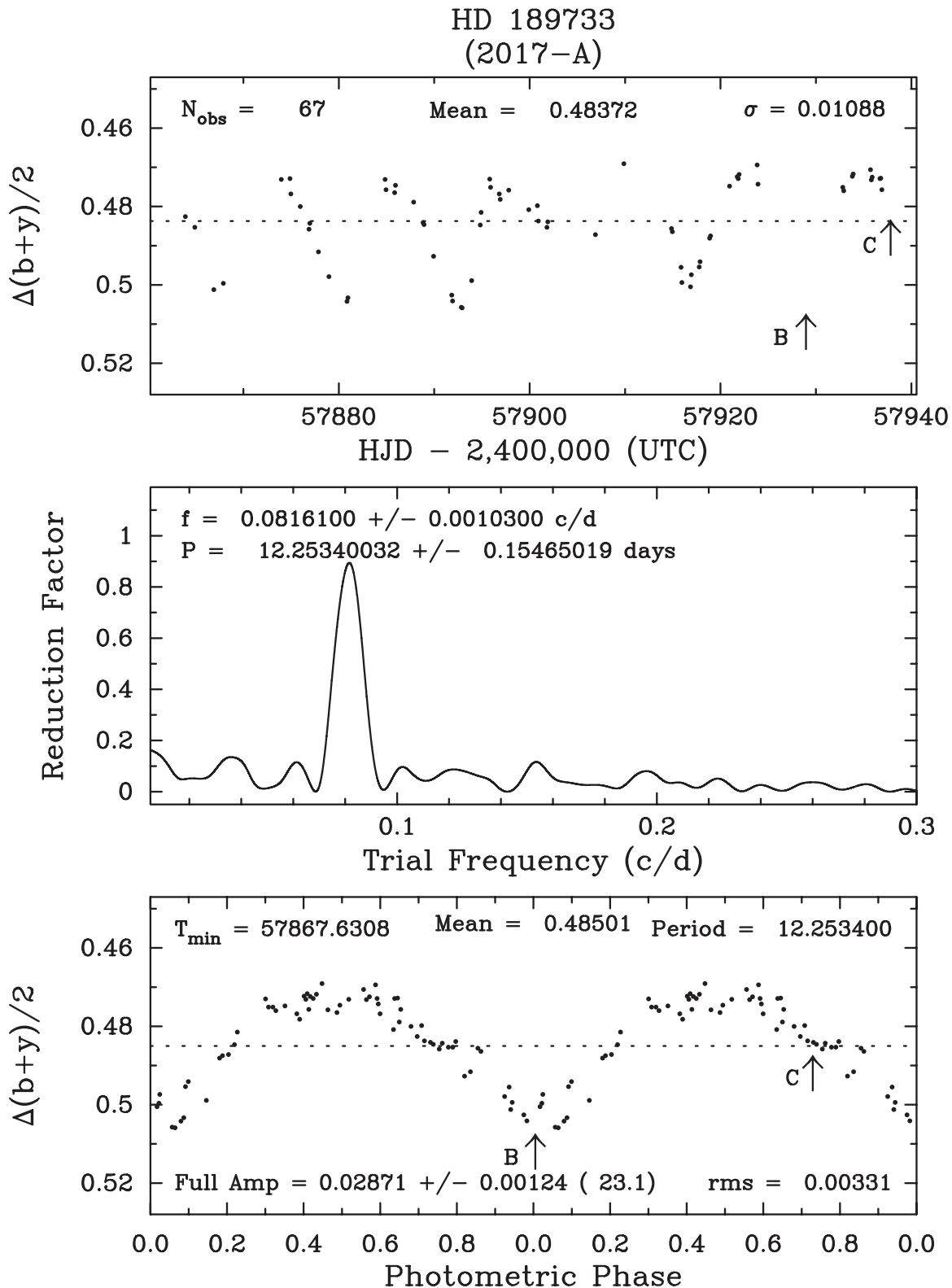


Figure 14. Top panel: ground-based differential photometry of HD 189733 in the epoch of 2017A. Middle panel: frequency spectrum of the rotational modulation of HD 189733. Bottom panel: same as top panel, but phase-folded to the rotational period. The times corresponding to Visits B and C are marked with arrows.

observations, we combine the differential b and y magnitudes into a single pseudo-bandpass $(b + y)/2$. The typical precision of a single observation, as measured from pairs of constant comparison stars, typically ranges between 0.0010 and 0.0015 mag on good nights. The T8 APT, which is identical to T10, is described in Henry (1999).

We show the differential photometry of HD 189733 from season 2017A in Figure 14 (top and bottom panels). Visits B and C, which are the ones discussed in this manuscript, are marked with arrows. Visit B occurred when HD 189733 was in a light-curve minimum and therefore the most spotted phase. Visit C occurred after the following maximum when the star was approximately 0.025 mag brighter than during Visit B, and therefore less spotted. We identify a rotational period of 12.25 ± 0.15 days in the middle panel of Figure 14.

Appendix D

Extension of p-winds for Exospheric C and O

The isothermal, one-dimensional Parker wind code `p-winds` was originally developed to simulate transmission spectra of metastable He in the upper atmosphere of evaporating exoplanets (Dos Santos et al. 2022; Kirk et al. 2022; Vissapragada et al. 2022a). In the current development version (1.4.3), we implemented the modules `carbon` and `oxygen` that can calculate the distribution of neutral, singly ionized, and doubly ionized C nuclei, as well as neutral and singly ionized O nuclei. Future versions of the code will include other species relevant for observations of atmospheric escape, such as Si, Fe, and Mg. The development version of

`p-winds` also implements Roche lobe effects, as described in Vissapragada et al. (2022b) and Erkaev et al. (2007).

A list of the new reactions implemented on `p-winds` to allow the modeling of C and O is shown in Table 5; these are in addition to the reactions described in Dos Santos et al. (2022). To calculate the photoionization rates Φ as a function of the radius r , we use the following equation:

$$\Phi(r) = \int_0^{\lambda_0} \frac{\lambda}{hc} f_\lambda \sigma_\lambda e^{-\tau_\lambda(r)} d\lambda, \quad (D1)$$

where λ_0 is the wavelength corresponding to the ionization energy of a given species, and f_λ is the incident flux density. σ_λ is the photoionization cross section taken from the references listed in Table 5. τ_λ is the optical depth for a given species and is calculated as follows:

$$\tau_\lambda(r) = \int_r^\infty \sigma_\lambda n(r) dr, \quad (D2)$$

where n is the number density of a given species.

Following the formulation of Oklopčić & Hirata (2018), we calculate the fractions of ionized C and O using the steady-state advection and ionization balance combined with mass conservation to obtain the following equations:

$$\begin{aligned} v(r) \frac{df_{C\text{II}}}{dr} = & f_{C\text{I}} (\Phi_{C\text{I}} e^{-\tau_{C\text{I}}} + n_e q_{E\text{I}} + n_{\text{HII}} q_{T2} + n_{\text{HeII}} q_{T4}) \\ & - f_{C\text{II}} (n_e q_{R2} + n_{\text{HII}} q_{T1}) \\ & + f_{C\text{III}} (n_e q_{R3} + n_{\text{HII}} q_{T3} + n_{\text{HeI}} q_{T5}), \end{aligned} \quad (D3)$$

Table 5
New Reactions Used to Calculate the Distribution of O and C

Reaction	Rate ($\text{cm}^3 \text{s}^{-1}$)	References	
Photoionization			
P1	$\text{He} + h\nu \rightarrow \text{He}^+ + e$	See text	
P2	$\text{C} + h\nu \rightarrow \text{C}^+ + e$	See text	
P3	$\text{C}^+ + h\nu \rightarrow \text{C}^{2+} + e$	See text	
P4	$\text{O} + h\nu \rightarrow \text{O}^+ + e$	See text	
Recombination			
R1	$\text{He}^+ + e \rightarrow \text{He} + h\nu$	$4.6 \times 10^{-12} (300/T_e)^{0.64}$	Storey & Hummer (1995)
R2	$\text{C}^+ + e \rightarrow \text{C} + h\nu$	$4.67 \times 10^{-12} (300/T_e)^{0.60}$	Woodall et al. (2007)
R3	$\text{C}^{2+} + e \rightarrow \text{C}^+ + h\nu$	$2.32 \times 10^{-12} (1000/T_e)^{0.645}$	Aldrovandi & Pequignot (1973)
R4	$\text{O}^+ + e \rightarrow \text{O} + h\nu$	$3.25 \times 10^{-12} (300/T_e)^{0.66}$	Woodall et al. (2007)
Electron impact ionization			
E1	$\text{C} + e \rightarrow \text{C}^+ + e + e$	$6.85 \times 10^{-8} \left(\frac{1}{0.193 + U} \right)^{0.25} \exp(-U)$, $U = 11.3/E_e$ (eV)	Voronov (1997)
E2	$\text{C}^+ + e \rightarrow \text{C}^{2+} + e + e$	$1.86 \times 10^{-8} \left(\frac{1}{0.286 + U} \right)^{0.24} \exp(-U)$, $U = 24.4/E_e$ (eV)	Voronov (1997)
E3	$\text{O} + e \rightarrow \text{O}^+ + e + e$	$3.59 \times 10^{-8} \left(\frac{1}{0.073 + U} \right)^{0.34} \exp(-U)$, $U = 13.6/E_e$ (eV)	Voronov (1997)
Charge transfer with H and He nuclei			
T1	$\text{C}^+ + \text{H} \rightarrow \text{C} + \text{H}^+$	$6.30 \times 10^{-17} (300/T)^{-1.96} \exp(-170000/T)$	Stancil et al. (1998)
T2	$\text{C} + \text{H}^+ \rightarrow \text{C}^+ + \text{H}$	$1.31 \times 10^{-15} (300/T)^{-0.213}$	Stancil et al. (1998)
T3	$\text{C}^{2+} + \text{H} \rightarrow \text{C}^+ + \text{H}^+$	$1.67 \times 10^{-4} (10000/T)^{-2.79} [1 + 304.72 e^{(-4.07 T/10000)}]$	Kingdon & Ferland (1996)
T4	$\text{C} + \text{He}^+ \rightarrow \text{C}^+ + \text{He}$	$2.50 \times 10^{-15} (300/T)^{-1.597}$	Glover & Jappsen (2007)
T5	$\text{C}^{2+} + \text{He} \rightarrow \text{C}^+ + \text{He}^+$	$\sim 1.23 \times 10^{-9}$ for $T < 15,000$ K	Brown (1972)
T6	$\text{O}^+ + \text{H} \rightarrow \text{O} + \text{H}^+$	$5.66 \times 10^{-10} (300/T)^{-0.36} \exp(8.6/T)$	Woodall et al. (2007)
T7	$\text{O} + \text{H}^+ \rightarrow \text{O}^+ + \text{H}$	$7.31 \times 10^{-10} (300/T)^{-0.23} \exp(-226/T)$	Woodall et al. (2007)

Note. T_e is the temperature of the electrons, which we assume to be the same as the temperature of the outflow T . E_e is the energy of the colliding electrons at a given temperature T_e .

$$v(r) \frac{df_{C\text{II}}}{dr} = f_{C\text{II}} (\Phi_{C\text{II}} e^{-\tau_{C\text{II}}} + n_e q_{E2}) - f_{C\text{III}} (n_e q_{R3} + n_{H\text{I}} q_{T3} + n_{He\text{I}} q_{T5}), \quad (\text{D4})$$

$$v(r) \frac{df_{O\text{I}}}{dr} = f_{O\text{I}} (\Phi_{O\text{I}} e^{-\tau_{O\text{I}}} + n_e q_{E3} + n_{H\text{II}} q_{T7}) - f_{O\text{II}} (n_e q_{R4} + n_{H\text{I}} q_{T6}), \quad (\text{D5})$$

where f is the ionization fraction of a given species, q is the rate for a given reaction in Table 5, n is the number density of a given particle, $f_{C\text{I}} = 1 - f_{C\text{II}} - f_{C\text{III}}$, and $f_{O\text{I}} = 1 - f_{O\text{II}}$. Equations (D3) and (D4) are coupled and solved simultaneously using the ODEINT method of SciPy's (Virtanen et al. 2020) `integrate` module; Equation (D5) is solved using the IVP method of the same module. The first solutions are obtained from an initial guess of the fractions f provided by the user and then repeated until they reach a convergence of 1%.

The number densities as a function of the altitude for C II and O I are calculated as:

$$n_{C\text{II}}(r) = f_{C\text{II}}(r) \frac{f_C \rho(r)}{(f_H + 4f_{He} + 12f_C) m_H} \quad \text{and} \quad (\text{D6})$$

$$n_{O\text{I}}(r) = f_{O\text{I}}(r) \frac{f_O \rho(r)}{(f_H + 4f_{He} + 16f_O) m_H}, \quad (\text{D7})$$

where f_X is the total fraction of X nuclei in the outflow.

We then proceed to calculate the wavelength-dependent transmission spectrum by assuming that the only source of opacity in the atmosphere are the ions C II and C III and the O I atoms. We use the same simplified ray-tracing and line-broadening descriptions from Dos Santos et al. (2022). The central wavelengths, oscillator strengths, and Einstein coefficients of the spectral lines were obtained from the National Institute of Standards and Technology (NIST) database (Kramida et al. 2022).²⁰

The C II lines are composed of one transition arising from the ground state and a blended doublet arising from the first excited state (with an energy of 0.00786 eV); the three O I lines present in the COS spectra arise from the ground, first excited, and second excited states. As the equations above do not take excitation into account, we calculate the population of excited states using the CHIANTI software (version 10.0.2; Dere et al. 1997; Del Zanna et al. 2021) implemented in the ChiantiPy Python package²¹ (version 0.14.1; Landi et al. 2012). We assume that the upper atmosphere is isothermal and calculate the excited-state populations as a function of the electron number density. We then multiply the fraction of each state estimated by CHIANTI by the total number densities of C II and O I, which are used to calculate the transmission spectra.

ORCID iDs

Leonardo A. Dos Santos  <https://orcid.org/0000-0002-2248-3838>

Antonio García Muñoz  <https://orcid.org/0000-0003-1756-4825>

David K. Sing  <https://orcid.org/0000-0001-6050-7645>

Mercedes López-Morales  <https://orcid.org/0000-0003-3204-8183>

²⁰ <https://www.nist.gov/pml/atomic-spectra-database>

²¹ <https://github.com/chianti-atomic/ChiantiPy/>

Munazza K. Alam  <https://orcid.org/0000-0003-4157-832X>
 Vincent Bourrier  <https://orcid.org/0000-0002-9148-034X>
 David Ehrenreich  <https://orcid.org/0000-0001-9704-5405>
 Gregory W. Henry  <https://orcid.org/0000-0003-4155-8513>
 Thomas Mikal-Evans  <https://orcid.org/0000-0001-5442-1300>
 Nikolay K. Nikolov  <https://orcid.org/0000-0002-6500-3574>
 Jorge Sanz-Forcada  <https://orcid.org/0000-0002-1600-7835>
 Hannah R. Wakeford  <https://orcid.org/0000-0003-4328-3867>

References

- Addison, B., Wright, D. J., Wittenmyer, R. A., et al. 2019, *PASP*, **131**, 115003
 Aldrovandi, S. M. V., & Pequignot, D. 1973, *A&A*, **25**, 137
 Astropy Collaboration, Price-Whelan, A. M., Sipőcz, B. M., et al. 2018, *AJ*, **156**, 123
 Barth, P., Helling, C., Stüeken, E. E., et al. 2021, *MNRAS*, **502**, 6201
 Ben-Jaffel, L., & Ballester, G. E. 2013, *A&A*, **553**, A52
 Bonomo, A. S., Desidera, S., Benatti, S., et al. 2017, *A&A*, **602**, A107
 Bouchy, F., Udry, S., Mayor, M., et al. 2005, *A&A*, **444**, L15
 Bourrier, V., dos Santos, L. A., Sanz-Forcada, J., et al. 2021, *A&A*, **650**, A73
 Bourrier, V., Ehrenreich, D., Lecavelier des Etangs, A., et al. 2018, *A&A*, **615**, A117
 Bourrier, V., & Lecavelier des Etangs, A. 2013, *A&A*, **557**, A124
 Bourrier, V., Lecavelier des Etangs, A., Dupuy, H., et al. 2013, *A&A*, **551**, A63
 Bourrier, V., Wheatley, P. J., Lecavelier Des Etangs, A., et al. 2020, *MNRAS*, **493**, 559
 Brown, R. L. 1972, *ApJ*, **174**, 511
 Cauley, P. W., Kuckein, C., Redfield, S., et al. 2018, *AJ*, **156**, 189
 Cruz Aguirre, F., Youngblood, A., France, K., & Bourrier, V. 2023, *ApJ*, **946**, 98
 Cubillos, P. E., Fossati, L., Koskinen, T., et al. 2023, *A&A*, **671**, A170
 Del Zanna, G., Dere, K. P., Young, P. R., & Landi, E. 2021, *ApJ*, **909**, 38
 Dere, K. P., Landi, E., Mason, H. E., Monsignori Fossi, B. C., & Young, P. R. 1997, *A&AS*, **125**, 149
 Dos Santos, L. A., Ehrenreich, D., Bourrier, V., et al. 2019, *A&A*, **629**, A47
 Dos Santos, L. A., Vidotto, A. A., Vissapragada, S., et al. 2022, *A&A*, **659**, A62
 Ehrenreich, D., Bourrier, V., Wheatley, P. J., et al. 2015, *Natur*, **522**, 459
 Erkaev, N. V., Kulikov, Y. N., Lammer, H., et al. 2007, *A&A*, **472**, 329
 Fortney, J. J., Dawson, R. I., & Komacek, T. D. 2021, *JGRE*, **126**, e06629
 Fossati, L., Haswell, C. A., Froning, C. S., et al. 2010, *ApJL*, **714**, L222
 Gaia Collaboration, Brown, A. G. A., Vallenari, A., et al. 2018, *A&A*, **616**, A1
 García Muñoz, A. 2007, *P&SS*, **55**, 1426
 García Muñoz, A., Fossati, L., Youngblood, A., et al. 2021, *ApJL*, **907**, L36
 Glover, S. C. O., & Jappsen, A. K. 2007, *ApJ*, **666**, 1
 Gray, R. O., Corbally, C. J., Garrison, R. F., McFadden, M. T., & Robinson, P. E. 2003, *AJ*, **126**, 2048
 Green, J. C., Froning, C. S., Osterman, S., et al. 2012, *ApJ*, **744**, 60
 Harris, C. R., Millman, K. J., van der Walt, S. J., et al. 2020, *Natur*, **585**, 357
 Henry, G. W. 1999, *PASP*, **111**, 845
 Hundhausen, A. J. 1997, *Cosmic Winds and the Heliosphere* (Tucson, AZ: Univ. Arizona Press), 259
 Hunter, J. D. 2007, *CSE*, **9**, 90
 Ito, Y., & Ikoma, M. 2021, *MNRAS*, **502**, 750
 Johnson, C. I., Plesha, R., Jedrzejewski, R., Frazer, E., & Dashtamirova, D. 2021, *Updated Flux Error Calculations for CalCOS*, Instrument Science Report COS 2021-03
 Kingdon, J. B., & Ferland, G. J. 1996, *ApJS*, **106**, 205
 Kirk, J., Dos Santos, L. A., López-Morales, M., et al. 2022, *AJ*, **164**, 24
 Kluyver, T., Ragan-Kelley, B., Pérez, F., et al. 2016, in *Positioning and Power in Academic Publishing: Players, Agents and Agendas*, ed. F. Loizides & B. Schmidt (Amsterdam: IOS Press), 87
 Koskinen, T. T., Harris, M. J., Yelle, R. V., & Lavvas, P. 2013, *Icar*, **226**, 1678
 Kramida, A., Ralchenko, Y., Reader, J., & NIST ASD Team 2022, *NIST Atomic Spectra Database* (ver. 5.10) (Gaithersburg, MD: National Institute of Standards and Technology), <https://physics.nist.gov/asd>
 Kreidberg, L. 2015, *PASP*, **127**, 1161
 Lampón, M., López-Puertas, M., Sanz-Forcada, J., et al. 2021, *A&A*, **647**, A129
 Landi, E., Del Zanna, G., Young, P. R., Dere, K. P., & Mason, H. E. 2012, *ApJ*, **744**, 99

- Lecavelier Des Etangs, A., Bourrier, V., Wheatley, P. J., et al. 2012, *A&A*, **543**, L4
- Lecavelier Des Etangs, A., Ehrenreich, D., Vidal-Madjar, A., et al. 2010, *A&A*, **514**, A72
- Lecavelier Des Etangs, A., Pont, F., Vidal-Madjar, A., & Sing, D. 2008, *A&A*, **481**, L83
- Linsky, J. L., Bushinsky, R., Ayres, T., Fontenla, J., & France, K. 2012, *ApJ*, **745**, 25
- Loyd, R. O. P., & France, K. 2014, *ApJS*, **211**, 9
- Madhusudhan, N., Crouzet, N., McCullough, P. R., Deming, D., & Hedges, C. 2014, *ApJL*, **791**, L9
- McCullough, P. R., Crouzet, N., Deming, D., & Madhusudhan, N. 2014, *ApJ*, **791**, 55
- Nakayama, A., Ikoma, M., & Terada, N. 2022, *ApJ*, **937**, 72
- Odert, P., Erkaev, N. V., Kislyakova, K. G., et al. 2020, *A&A*, **638**, A49
- Oklopčić, A., & Hirata, C. M. 2018, *ApJL*, **855**, L11
- Owen, J. E. 2019, *AREPS*, **47**, 67
- Owen, J. E., Murray-Clay, R. A., Schreyer, E., et al. 2023, *MNRAS*, **518**, 4357
- Parker, E. N. 1958, *ApJ*, **128**, 664
- Pillitteri, I., Micela, G., Maggio, A., Sciortino, S., & Lopez-Santiago, J. 2022, *A&A*, **660**, A75
- Rumenskikh, M. S., Shaikhislamov, I. F., Khodachenko, M. L., et al. 2022, *ApJ*, **927**, 238
- Salz, M., Czesla, S., Schneider, P. C., et al. 2018, *A&A*, **620**, A97
- Salz, M., Czesla, S., Schneider, P. C., & Schmitt, J. H. M. M. 2016a, *A&A*, **586**, A75
- Salz, M., Schneider, P. C., Czesla, S., & Schmitt, J. H. M. M. 2016b, *A&A*, **585**, L2
- Sanz-Forcada, J., Micela, G., Ribas, I., et al. 2011, *A&A*, **532**, A6
- Sanz-Forcada, J., Ribas, I., Micela, G., et al. 2010, *A&A*, **511**, L8
- Sing, D. K., Fortney, J. J., Nikolov, N., et al. 2016, *Natur*, **529**, 59
- Sing, D. K., Lavvas, P., Ballester, G. E., et al. 2019, *AJ*, **158**, 91
- Sing, D. K., Pont, F., Aigrain, S., et al. 2011, *MNRAS*, **416**, 1443
- Stancil, P. C., Havener, C. C., Krstić, P. S., et al. 1998, *ApJ*, **502**, 1006
- Storey, P. J., & Hummer, D. G. 1995, *MNRAS*, **272**, 41
- Verner, D. A., Ferland, G. J., Korista, K. T., & Yakovlev, D. G. 1996, *ApJ*, **465**, 487
- Vidal-Madjar, A., Désert, J. M., Lecavelier des Etangs, A., et al. 2004, *ApJL*, **604**, L69
- Vidal-Madjar, A., Lecavelier des Etangs, A., Désert, J. M., et al. 2003, *Natur*, **422**, 143
- Virtanen, P., Gommers, R., Oliphant, T. E., et al. 2020, *NatMe*, **17**, 261
- Vissapragada, S., Knutson, H. A., dos Santos, L. A., Wang, L., & Dai, F. 2022a, *ApJ*, **927**, 96
- Vissapragada, S., Knutson, H. A., Greklek-McKeon, M., et al. 2022b, *AJ*, **164**, 234
- Voronov, G. S. 1997, *ADNDT*, **65**, 1
- Watson, A. J., Donahue, T. M., & Walker, J. C. G. 1981, *Icar*, **48**, 150
- Woodall, J., Agúndez, M., Markwick-Kemper, A. J., & Millar, T. J. 2007, *A&A*, **466**, 1197
- Yan, M., Sadeghpour, H. R., & Dalgarno, A. 1998, *ApJ*, **496**, 1044
- Yee, S. W., Winn, J. N., & Hartman, J. D. 2021, *AJ*, **162**, 240
- Zhang, M., Cauley, P. W., Knutson, H. A., et al. 2022, *AJ*, **164**, 237
- Zhang, M., Chachan, Y., Kempton, E. M. R., Knutson, H. A., & Chang, W. H. 2020, *ApJ*, **899**, 27
- Zhu, W., & Dong, S. 2021, *ARA&A*, **59**, 291